UNIVERSITÀ DEGLI STUDI DI NAPOLI
FEDERICO II

UNIVERSITÀ DEGLI STUDI DI NAPOLI FEDERICO II

PH.D. THESIS

IN

MEASUREMENTS

NON-DESTRUCTIVE TESTING (NDT)

METHODS BASED ON

TERAHERTZ RADIATION AND

COMPRESSIVE SAMPLING

GIOVANNI CAVALLO

TUTOR: PROF. ANNALISA LICCARDO

COORDINATOR: PROF. DANIELE RICCIO

XXX CICLO

SCUOLA POLITECNICA E DELLE SCIENZE DI BASE
DIPARTIMENTO DI INGEGNERIA ELETTRICA E TECNOLOGIE DELL'INFORMAZIONE

TESI DI DOTTORATO

UNIVERSITÀ DEGLI STUDI DI NAPOLI "FEDERICO II"

DIPARTIMENTO DI INGEGNERIA ELETTRICA E
TECNOLOGIE DELL'INFORMAZIONE

DOTTORATO DI RICERCA IN
INFORMATION TECHNOLOGY AND ELECTRICAL ENGINEERING

NON-DESTRUCTIVE TESTING METHODS BASED ON TERAHERTZ RADIATION AND COMPRESSIVE SAMPLING

GIOVANNI CAVALLO

Il Coordinatore del Corso di Dottorato	Il Tutore
Ch.mo Prof. Daniele RICCIO	Ch.mo Prof. Annalisa LICCARDO

A. A. 2016–2017

Contents

List of Figures

Introduction

Cracks and defects can significantly influence the performance of components and structures to such an extent that their identification is an essential part of quality control in all fields of engineering. The set of techniques and procedures that have as their purpose the evaluation of defects in the materials or artifacts is generally classified under the name of 'Non-destructive Testing' (NDT) or 'Non-destructive Evaluation' (NDE). However, NDT applications often go far beyond the simple detection and localization of defects, because they relate to all aspects of the characterization of solids, the study of their micro-structure and morphology, the analysis of physical-chemical, their preparation methods, and so on. NDT techniques typically include X-ray, ultrasonic, penetrating liquid inspection, magnetic particle method (magnetoscopy), thermography and visual inspection. NDT techniques can be applied to both metallic and non-metallic materials and to objects of different dimensions both static and in motion, but the common point to all is their ability to not affect the physical-mechanical characteristics of the tested component in any way; this means that, unlike many of the tests usually used to characterize materials (as traction tests) that involve partial or total destruction of the specimen, non-destructive controls don't alter the workability of the piece, which can be safely put into operation (when it is not possible to test it in-situ) immediately after testing. It is important to observe that the optimal solution obtained by NDT tests is a combination of compromise solutions that put into play different aspects as costs, user ability, sensitivity, safety and so on. The only existence of a wide variety of NDT methods suggests that none of the techniques are in themselves complete, but rather they constitute a set in which each one is more suitable than others under certain circumstances, or (as usual) more methods are used in a complementary way to control the same product to ensure that as many potential defects are as possible. Although many classifications have been proposed for the division of techniques into homogeneous classes, the boundary between the performances that each

method can offer is somewhat ambiguous. However, a wide-ranging classification can be made by separating the 'volumetric' and 'superficial' controls: in the first case (X-rays, ultrasounds) it is possible to investigate the internal defects of the component, while in the second (Magnetoscopy, Penetrating Visual Inspection) the technique merely provides information on surface defects or sub- superficial. Sometimes, as in the case of the ultrasonic method, for example, it is possible to detect both defect classes, but generally this technique is most often used for internal control. Another conditioning factor can be related to the type of material tested. Not all the methods are equally well suited to investigating the wide range of materials used in the various engineering sectors. For example, the magnetic particles method can only be applied to ferromagnetic or conductive materials, and this excludes a priori all classes of non-metallic plastic or rubbery materials. This problem is not found, however, if ultrasounds are used, which, being elastic waves, require only a medium (solid or liquid) to propagate.

Therefore, besides the above-mentioned methods as X-ray, ultrasonic radiology and magnetoscopy, it is possible to consider two additional investigative methods, as THz radiation and 'Eddy Currents Testing' (ECT).

THz radiation method is based on the use of high-frequency radiation, and it is also called T-waves. During the years, that technology has found an interesting attractiveness in different fields of both industry and academia sector thanks to their many important properties. First, they are not perceptible by the human eye, are not ionizing, and have the ability to cross many nonconducting common materials such as paper, fabrics, wood, plastic, and organic tissues. For this reason, THz radiation is of particular interest for spectroscopy and imaging operations, which are used in the most diverse fields of production and research. In this case, THz spectroscopy, which allows to study the electrodynamic properties of materials, such as permittivity, conductivity and absorption coefficient, etc., was used to carry out a study on composite materials such as carbon nanotubes (NTC). In particular, through the analysis of electrodynamic properties, the feasibility of shielded instruments at the frequencies of the T-waves for electromagnetic fields was evaluated. At the same time with THz Imaging, simple scans/analysis of sub-millimetric defects of different nature on composite materials of avionics nature (as kevlar and carbon fiber) were made by exploiting the Raster Scan (RS) technique. As it can be expected, RS technique provides excellent resolution, to the detriment of the measurement time; in particular, the higher the number of pixels involved in the image reconstruction, the higher the corresponding time required to ac-

quire the whole image.
To overcome the considered drawback, the exploitation of an alternative approach, referred to as Compressive Sampling (CS) has been proposed. In particular, CS allows to considerably reduce the measurement time, since it permits to reconstruct desired images by means of a lower number of measurements through the use of a set of suitable masks.
Unfortunately, the measurement time is reduced at the expense of the accuracy characterizing the reconstructed image; nevertheless, the accuracy required in tests for the defect detection is often lower than that assured by RS technique. In several cases, in fact, detection of defect or rough estimation of its size, without needing of precisely reconstructing its shape, turns out to be sufficient; if required, a successive RS approach could be applied for more accurate reconstruction. Finally, with regard to the performance assessment of the considered CS approach, a characterization of the CS-THz Imaging approach through an intense experimental campaign carried out on a traditional THz Time Domain System (TDS) is performed, in order to highlight problems affecting the experimental application of CS-based method focusing attention on some different uncertainty sources.

Nowadays, ECTs are considered among the different NCT techniques, because modern ECT techniques offer low-cost methods for high-speed large-scale inspection of metallic materials such as those used in nuclear, aerospace, and maritime applications where premature failures could give rise to economic problems and/or endanger human life. *NDT-ECT* can be divided into three steps, i.e., detection, location, and characterization. Detection is the ability to find the presence of a defect; location finds a specimen area where the defect is situated; and characterization allows both the shape and geometrical dimensions of the defect to be evaluated with acceptable uncertainty. On this basis, an acceptance/rejection decision is carried out by either a human operator or an automatic system. Typically, in the ECT field, component selection is carried out by expert human operators that decide the acceptability of the piece under test by evaluating useful quantities such as typical 2-D graphs that show the behavior of the reactance versus the resistance of the impedance response of the ECT probe (the measured impedance plane). Modern instruments are able to automatically select the defect by using, for example, a comparator, which analyzes the measured signal with reference to a suitable threshold. These instruments often require large amounts of memory to store and save the acquired data. Indeed, it is common to divide the various survey areas into micro structures, each of which is in turn considered to be a sub-pixel struc-

ture. For each pixel, according to the theory of ECT, it is necessary to acquire two signals that the probes can detect, i.e voltage and current, necessary to extract the information necessary to confirm the presence or not of the defect inside the structure. The disadvantage lies in the fact that electrical signals are captured with a very large number of samples, about 100.000 samples for pixel, taking into account the time needed to capture all these samples. For this reason, the CS approach has been introduced to reduce the amount of data to be captured and stored in the memory slots, but at the same time to reduce the acquisition and subsequent reconstruction of the signal. To do this, two CS-solvers are presented, in particular the Matching Pursuit (MP) and Compressive Sampling Matching Pursuit $(CoSaMP)$, which are also alongside by graphics solutions as *Compute Unified Device Architecture*, so-called $(CUDA)$ and *Graphic Processing Unit*, so called (GPU).

Chapter 1

State of Art

1.1 Terahertz Radiation

Terahertz radiation, also called T-waves, refers to the frequency domain ranging approximately from 100 GHz to 10 THz, corresponding to wavelengths from 3 mm to 30 μm. The lower limit is the microwave region, where mobile and satellite systems operate, and the upper limit is the far infrared, widely used for optical communications. In Fig. 1.1 the characteristics of the T-waves in the electromagnetic spectrum are shown.

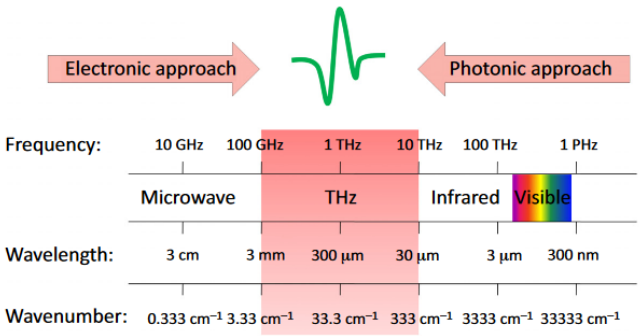

Figure 1.1: Position of the THz waves in the EM spectrum.

Terahertz frequency region is often defined as the last unexplored area of the EM spectrum, since it represents an area of convergence between electronics and photonics presently lacking a mature technology. Since T-waves are located between microwaves and far-infrared waves, there are two enabling

technologies that can be considered for their full exploitation: electronics and photonics. Over the past 20 years, the full access and exploitation of this frequency window have been the objective of intense research efforts both in academia and in industry, in order to close the so-called THz gap. T-waves present many important properties potentially with a shattering impact both in science and in many real-world applications. First, they are not perceptible by the human eye, are not ionizing, and have the ability to cross many nonconducting common materials such as paper, fabrics, wood, plastic, and organic tissues. [3], [4]

Since the seventies, THz technology has been studied and exploited in fields as astronomy and pharmaceutical industry. Nevertheless, recent scientific innovations have contributed to farther explore THz systems in other sectors. Nowadays, THz radiation finds use in a wide range of applications, as for example [5] − [7]:

a. Non destructive and non invasive analysis

b. Security and National Defense

c. Industrial, chemical and biological products

Because of the excellent properties exhibited by radiation in this frequency (energy) range, THz Spectroscopy and THz imaging are the main applications of THz technology, in fact, in terms of energy, they give access to the rotational and vibrational modes of many molecules and macro-molecules. These modes can be observed as absorption peaks in the THz spectra, providing the *fingerprint* of unknown compounds. Futhermore, the use of THz radiation allows contactless and non-destructive analysis of the materials under investigation, by spatial imaging operations [5], [8] with resolution higher than micro and millimeter waves, for that THz science can be applied in so many and different areas of interest, from biology to physical, chemical, and environmental research, within a broad range of industries including the medical, security, cultural heritage, manufacturing, and aerospace sectors.

In the field of cultural heritage, studies and diagnostic activities on masterpieces are of paramount importance, as a scientific tool, which is a precautionary measure for conservation and recovery. Nevertheless, they must be dealt with extreme caution in order not to compromise the delicate balance of the work itself, for example *ENEA*, thanks to its experience in the field of technologies applied to the preservation and recovery of cultural heritage, has allowed the development of non-invasive tools and methodologies that do not compromise the integrity of the work.

In the field of security applications: every amazing substance and every explosive has a distinctive trace that uniquely characterizes it in the spectrum of THz. These traces allow the identification of many chemicals through their spectrum of transmission and reflection: it is possible to identify illegal substances such as drugs or explosives among other harmless contents. All this is possible because the waves are below 3.0 THz and can cross the packaging with low attenuation, and identify and locate materials without opening the enclosure [4], [9]. Today, however, the security problem has become crucial even in airports where there are no tools to do so. Among these, it is possible to consider the body scanner, or a cabin inside which the person is accommodated to be analyzed, Fig. 1.2. This device allows the human body to be scanned through a sub-millimeter (30-300 GHz) wavelength radiation that in the electromagnetic spectrum corresponds to the transition range between the microwaves and the THz, allowing for detection without any physical search, dangerous objects or explosives.

Figure 1.2: A typical body scanners working at T-waves that could be installed in airport

THz radiation has played a primary role, also, in the medical field but above all in pharmaceutical one. In the past, the pharmaceutical industry carried out finished products and then carried out laboratory tests to verify the quality of the finished product, with the disadvantage that if the final product could not meet the specifications, the entire game was destroyed. The following was used in the process *Process Analytical Technology* (*PAT*), which was used during the whole drug production process, from raw material to sale, al-

lowing you to have real-time information on the drugs that were in production [5], [9]. The *PAT* technique was replaced by THz spectroscopy which was more relevant than analytical technique because it allows a non-destructive test of product stability inside the container to be carried out, improving the quality and uniformity of the product itself. Finally, THz spectroscopy and imaging are also used for cancer diagnosis [9], [10] . The absorption of Terahertz waves, being sensitive to polar molecules, such as water, allows to identify cancerous tissues. In addition, cancer cells can also be detected in frozen tissues as the THz frequency transmission is much higher than that of water.

1.1.1 THz systems

About THz system, two different approaches to perform evaluation, referred respectively to as Time Domain (TD) and Continuous Wave (CW), can be considered. The choice between them depends on two important issues as emission mode and operating frequency [11].

Time domain THz systems

A standard TD-THz system, shown in Fig. 1.3, is composed of an ultrafast ($<$ 100 fs) optical laser, a T-ray emitter, a set of mirrors and an optical delay line, and a THz receiver. The sample is placed between the THz emitter and the detector. These systems are broadband in nature and their emission is not continuous, so it is possible to realize measurements in both transmission and reflection mode for spectroscopic applications. In TD-THz systems, the distinctive element is an optical-to-THz signal conversion technology, based on the generation and detection of an electromagnetic transient having duration of few picoseconds by means of ultrafast pulsed lasers [12], and then by Fourier transformation, frequency components in the 0.1-5 THz can be retrieved [11].

The ultrafast optical pulse is divided by a beam splitter into two paths, to give a pump beam and a probe beam. The optical pump beam stimulates T-ray pulsed radiation (1-2 ps) from the emitter, that is usually a photoconductive antenna. In the configuration shown in Fig. 1.3 (transmission mode), a set of lenses and a parabolic mirror permit to the diverging T-ray beam to be collimated and focuses onto the sample. A set of lenses and mirror, identical to those near the emitter, permit to the T-ray beam to be re-collimated and focused onto the receiver, after T-ray is passed through the sample. To realize the detection, either charge transport or optical rectification effect can be considered, depending on the type of receiver that is used. The probe beam optically gates

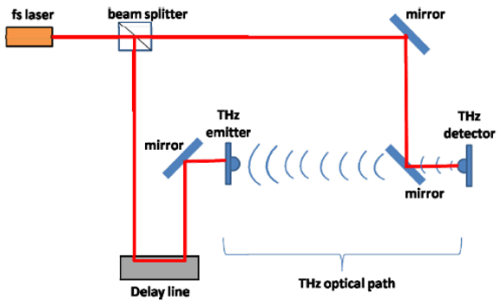

Figure 1.3: Traditional scheme of a TD-THz system

the T-ray receiver with a pulse much shorter than the arriving T-ray signal duration. The synchronization between the optical probe pulse and the T-ray pulse allows the coherent detection of the T-ray signal at a defined time instance. By means of discrete micro-motion of the mechanical stage controlling the optical delay line, different instants of the impinging T-ray signal can be gated, obtaining, thus, a complete temporal scan of the T-ray signal. Finally, the system is supported by a remote control station composed by a lock-in amplifier that permits to amplify the low signal detected by THz detector, and a personal computer to display and digitally process the THz signal [11].

Continuous Wave THz systems

A standard CW-THz system, shown in Fig. 1.4, is composed of a THz emitter, characterized for example, by a Quantum Cascade Laser (QCL), a very compact solid state THz emitter based on intersubband transitions in quantum wells of a semiconducting hetero-structure. These emitters can cover a THz range from 2 to 5 THz with a very small power output, in the range of mW. The main drawback of QCLs is the cryogenic condition (temperature within the range 4-100 K) needed for their operation. The QCL's radiation is collected and focused by a metallic ellipsoidal mirror, and then the detection is realized by a bolometer or pyro electric detector connected to a lock-in amplifier that this an integrated part of the remote control station [11].

CW-THz systems are very low tunable and basically narrow band, but provide very high spectral resolution and power output. The most important difference with TD-THz systems is that these systems works at a fixed frequency, while TDS works to different frequencies thanks to the application of Fourier transformation.

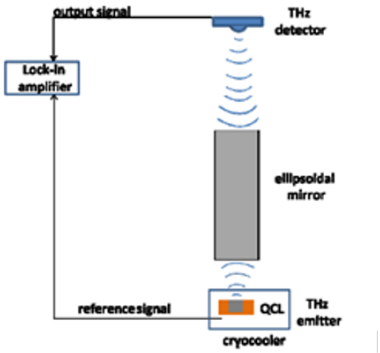

Figure 1.4: Traditional scheme of a CW-THz system

1.1.2 THz spectroscopy

The term spectroscopy refers to a series of experiments aiming to investigate the excited states of a specimen, exploiting the interaction of a proper electromagnetic perturbation with a sample. Reflected and/or transmitted waves release specific information on the electromagnetic properties of the sample as function of the frequency. Therefore, according to the spectral content of the electromagnetic signal-probe, different excitations can be investigated ranging from the quantum properties (energy levels of atomic bonds, roto-vibrational states etc.) of molecules to the impedance of a macroscopic samples or transmission lines. The THz band is ideal to study electrodynamic properties of materials from metals to insulators, since the frequency is lower than the typical plasma frequency of metals (about 10^{15} Hz) that defines the frequency above which the metal becomes transparent to radiation. Coherent THz radiation can provide valuable information on the complete set of the complex electrodynamic parameters [13] (refractive index ($\tilde{n}$) permittivity ($\tilde{\epsilon}$) and/or conductivity ($\tilde{\sigma}$)) characterizing a material whatever it is an insulator or metallic-like. The complex refractive index ($\tilde{n} = n + ik$) furnishes information on both the delay (n) and the absorption (k). Once n and k are obtained (see below) the permittivity $\tilde{\epsilon} = \epsilon_1 + i\epsilon_2$ can be reached exploiting the following relationship $\tilde{n} = \sqrt{\tilde{\epsilon}\tilde{\mu}/\epsilon_0\mu_0}$ where $\tilde{\mu}$ is the complex magnetic permeability, ϵ_0 is the vacuum permittivity and μ_0 is the vacuum permeability. Since most of materials have $\tilde{\mu} = 1$ a direct relation between the refractive index and permittivity can be extracted $\tilde{n} \cong \sqrt{\tilde{\epsilon}}$ which deals $n = \sqrt{(\sqrt{{\epsilon_1}^2 + {\epsilon_2}^2} + \epsilon_1)/2}$ and $k = \sqrt{(\sqrt{{\epsilon_1}^2 + {\epsilon_2}^2} - \epsilon_1)/2}$.

Conductivity ($\tilde{\sigma} = \sigma_1 + i\sigma_2$) and permittivity are also reciprocally related through the formulas $\sigma_1 = \epsilon_0\omega\epsilon_2$ and $\sigma_2 = \epsilon_0\omega(\epsilon_\infty - \epsilon_1)$, where $\omega = 2\pi\nu$ and $\epsilon_\infty = \epsilon(\omega \to \infty)$ can be obtained through a fitting procedure. From the practical point of view, the most important parameter to obtain for a sample characterization is $\tilde{n}$, since the other parameters are just a combination of *n* and *k*.

The peculiar characteristic of using a THz Time Domain Spectroscopy (TDS) system consists into directly manipulating the time dependent electric field $E(x,t)$ transmitted through the sample. The ratio between the Fourier transforms of the transmitted signal and the reference signal is directly function of the refractive index. The sketch of the measurement on a generic sample *L* thick is reported in Fig. 1.5. $E(x,t)$ propagating from the Transmitter (Tx) to the Receiver (Rx) is linearly polarized along y. Since the signal is generated and detected in air, the proposed scheme allows to generalize the measurements in multi-layer samples.

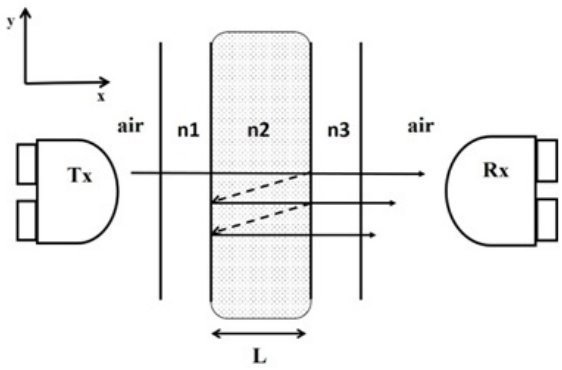

Figure 1.5: Scheme of the measurements through the THz-TDs system.*Tx* and *Rx* stand for transmitter and receiver, respectively. *L* represents the mean size of the sample, while n_i with i = 1, 2, 3 are the refractive index of different through THz pulse

The transmitted signal through the sample $S(\omega)$, can be expressed as function of the Fresnel coefficients $T_{a,b}(\omega) = 2\tilde{n}_a / (\tilde{n}_a + \tilde{n}_b)$ and $R_{a,b}(\omega) = (\tilde{n}_a - \tilde{n}_b) / (\tilde{n}_a + \tilde{n}_b)$ and the propagation factor $P_a(\omega, d) = exp\{-i\tilde{n}_a\omega d\}$, where the labels refer to the material [14]. The complete signal can be ex-

pressed as:

$$S(\omega) = \eta(\omega)\, T_{1,2}(\omega)\, P_2(\omega, d)\, T_{2,3}(\omega) \sum_{k=0}^{\infty} \{R_{2,3}(\omega)\, {P_2}^2(\omega, L)\, R_{2,1}(\omega)\}^k \cdot E(\omega) \tag{1.1}$$

where $E(\omega)$ is the generated THz pulse and $\eta(\omega)$ accounts for all the reflected and transmitted signals which do not reach Rx. In eq. 1.1 the factors $T_{1,2}(\omega)\, P_2(\omega, d)\, T_{2,3}(\omega) \sum_{k=0}^{\infty} \{R_{2,3}(\omega)$ take into account of the fraction of signal reaching Rx in one path, whereas the term $\sum_{k=0}^{K} \{R_{2,3}(\omega)\, {P_2}^2(\omega, L)\, R_{2,1}(\omega)\}^k$ accounts for the delayed K-pulses originated by the reflections of the primary pulse between the sample boundaries (usually $K \leq 3$).

This phenomenon known as Fabry-Perot (FP) effect is depicted in Fig. 1.5 through the dashed arrows displaying the reflected signals. In the time domain, the FP effects shows up in the appearance of copies of the primary transmitted signal. In Fig. 1.6 a comparison is proposed between the reference signal (air) and the signal (Si) through a silicon slab 500 μm thick. Black arrows point out the copies of the primary signal. The delay between copies is due to the roundtrip walk in the sample and is about $\Delta t \cong 2Ln/c \sim 11.4$ ps for $n(Si)$ = 3.46.

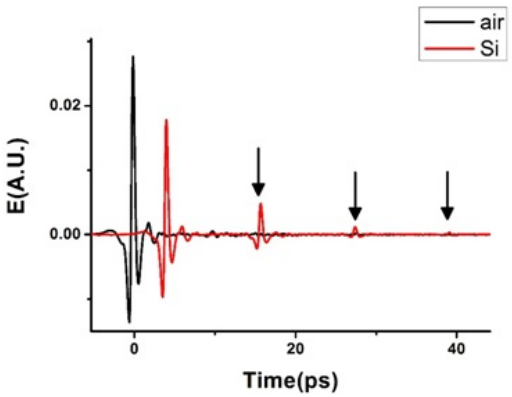

Figure 1.6: Time-dependent signal measured through THz-TDS system. The black curve is the reference signal acquired in free space, whereas the red curve is the signal through a Si sample of 500 μm thick. The black arrows indicate the primary signal copies generated by the Fabry Perot effect.

Eq. (1.1) also defines the trasmittance

$$T(\omega) = \frac{E_{sample}}{E_{ref}} \tag{1.2}$$

that according to eq.(1.1), in the case of a simple slab can be expressed as

$$H(\omega) = \frac{2\tilde{n}_2(\tilde{n}_1 + \tilde{n}_3)}{(\tilde{n}_2 + \tilde{n}_1)(\tilde{n}_2 + \tilde{n}_3)} exp\left\{-\frac{i(\tilde{n}_2 - \tilde{n}_{air})\omega L}{c}\right\} FP(\omega) \tag{1.3}$$

where

$$FP(\omega) = \frac{1}{1 - \left(\frac{\tilde{n}_2 - \tilde{n}_1}{\tilde{n}_2 + \tilde{n}_1}\right)\left(\frac{\tilde{n}_2 - \tilde{n}_3}{\tilde{n}_2 + \tilde{n}_3}\right) exp\{-i\tilde{n}_2\omega L/c\}} \tag{1.4}$$

is the explicit form of the Fabry-Perot tern when the echos in media 1 and 3 are negligible [14].

The transfer function $H(\omega)$ in eq. 1.3 is used as theoretical reference for $T(\omega)$ to calculate optical parameters of samples. Equations (2.1) and (1.3) describe the transmission through a homogeneous slab with refractive index $\tilde{n}_2$ when the equivalence $\tilde{n}_1 = \tilde{n}_3 = \tilde{n}_{air}$ is verified. Instead by putting $\tilde{n}_1 = \tilde{n}_{air}$, equations (2.1) and (1.3) are able to describe a system composed by two layers as a thin metallic film on a dielectric substrate [15], [16].

Several techniques [15] $-$ [19] have been developed in order to extract $\tilde{n}$ by computing the minimum difference between the modules and the phases of $H(\omega)$ and $T(\omega)$:

$$\begin{aligned} \delta\rho(\omega) &= |H(\omega)| - |T(\omega)| \\ \delta\varphi(\omega) &= arg[H(\omega)] - arg[T(\omega)] \end{aligned} \tag{1.5}$$

Equations (1.5) allow to define an error function, the Total Variation (TV) [17], defined by the sum of differences $\delta\rho$ and $\delta\varphi$ for each frequencial point

$$ER = \sum_{\omega} |\delta\rho(\omega)| + |\delta\varphi(\omega)| \tag{1.6}$$

This is a tridimensional paraboloid as function of the frequency and the sample thickness. The computational search of the minimum of $ER(L, \omega)$ implies the contemporary knowledge of the main quantities describing the system: the sample thickness, L the refractive index n and the extinction coefficient k [18]. A fast resolution of the TV approach is affected by the noise in the measured spectrum of $T(\omega)$. The most relevant noise source in thin

samples are the Fabry-Perot oscillations which shows a frequency inversely proportional to L. This problem can be overcame imposing the quasi space (QS) optimization [18], where the periodicity of the FP effect is employed to achieve the effective optical thickness of the sample. The quasi space is defined by the Fourier transform of an electro-dynamical parameter $y(\omega_n)$ which could be the refractive index or the extinction coefficient. Therefore a new set of variables can be defined as follows:

$$Q_{S_k} = \sum_{n=1}^{N-1} \left[y(\omega_n) \, exp\left(-i \frac{2\pi}{N} kn \right) \right], k = 0, 1, 2, ..., N-1 \tag{1.7}$$

This function can be displayed in terms of the variable $L_{Q_S} = x_{Q_S} c_0/2$, where c_0 is the speed of light in vacuum and $x_{Q_S} = 2\pi/\omega$, showing a pronounced peak at the effective optical length. Alternatively, the sample thickness L can be accounted by locating the minimum of Q_{S_k} (at a fixed frequency) for different L values [19]. The QS approach is limited just by the performances of the TDS system. In particular the maximum and minimum detectable thickness can be expressed as $L_{max} = c_0/4ndf$ and $L_{min} = c_0/2n\Delta f)$ where df is the minimum detectable frequency of the system while Δf is its bandwidth. The former thickness is based on the application of Nyquist theorem, whereas the latter is based on the resolution of neighbor *QS*'s peaks [19]. For instance, assuming as parameters $df \cong 3GHz$, $\Delta f \cong 3THz$ and, as effective refractive index, $n \cong 2$, the maximum and minimum length are $L_{max} \cong 12.5mm$ and $L_{min} \cong 12.5\mu m$ respectively. Whenever the best optical length is found, the quality of the retrieved electrodynamic parameter depends also by the choice of a good thickness of the sample. Thinner samples become transparent to THz radiation whereas thick samples do not release much information because the transmitted signal is low. In ref. [20] authors aim to find the best thickness in order to minimize the standard deviations $\left({s_n}^2, {s_k}^2\right)$ of electro-dynamical parameter as $n(\omega)$ and $k(\omega)$ inherited by the standard deviations of signals $E_{sample}(t)$ and $E_{ref}(t)$ acquired in the time domain. The functions ${s_n}^2$, ${s_k}^2$ can be minimized with respect L leading to get the optimal thickness as function of the absorption coefficient:

$$L_{opt} = c_0/\omega k(\omega) = \frac{2}{\alpha(\omega)} \tag{1.8}$$

Equation (1.8) shows that $n(\omega)$ and $k(\omega)$ are affected by some indetermination as consequence of the fixed extension of the sample. On the other hand,

eq. (1.8) enables the possibility to get reliable results also on very thin samples provided that the absorption coefficient $\alpha(\omega)$ is enough high. Indeed, full two dimensional systems like single graphene layers have been extensively investigated through THz-TDS systems thanks of the robust absorption coefficient $\alpha_{graphene} \sim 5\mu m^{-1}$ [21] $-$ [23].

1.1.3 THz Imaging

THz-based Imaging is gaining interest thanks to the fascinating characteristics of non-ionizing THz radiation of being able to pass through non-conductive materials [24],[25],[26], [27] such as wood, ceramic, plastic and similar, and so the demand for accurate non-destructive and non-invasive tests for the location of either superficial or bulk defects in materials is continuously growing [3].
The Imaging procedure consists in irradiating/illuminating the sample under test and acquiring the reflected/propagated radiation to reconstruct its digital reproduction, with specific regard to potential defects [5], [12]. The most used technique is the Raster Scan (RS), i.e. a system with a single source that generates the radiation that illuminates the sample according to a pixel by pixel pattern [28],[29] and a single point detector that receives radiation passed through the object, then the sample is moved to acquire the successive pixel [30]. As it can be expected, RS technique provides excellent resolution, to the detriment of the measurement time; in particular, the higher the number of pixels involved in the image reconstruction, the higher the corresponding time required to acquire the whole image.
Typically, THz System is disposed in a focused configuration and a scheme is shown in Fig. 1.7.

Generally, the ultra-fast optical pulse arrives to the THz emitter after a particular path, characterized by a beam splitter that gives a pump beam and a probe beam, some optical components (as mirrors) and a delay line. The optical pump beam stimulates T-ray pulsed radiation (1-2 ps) from the emitter, that is usually a photo-conductive antenna, arriving to a THz detector, after that THz pulse passes a set of lenses as shown in Fig. 1.7. Finally, the system is supported by a remote control station composed by a lock-in amplifier that permits to amplify the low signal detected by THz detector, and a personal computer to display and digitally process the THz signal.
The test object is collocated between THz emitter and detector, in such a way as the THz impinges on it in the first useful position (pixel). RS requires, then, to step-by-step (i.e. pixel by pixel) move the sample through a dual-axis

linear stepper motor before the THz receiver. The stepper motor is updated with a defined step according to the desired resolution, associated the adopted THz frequency and wave-front. The THz radiation is, in fact, first collimated and then focused on the target image and the effective area (and consequently the resolution) of the impinging ray strictly depends of the frequency of the adopted THz beam. the lower the resolution, the greater the acquisition time, the better the readability of the reconstructed image of the sample of interest.

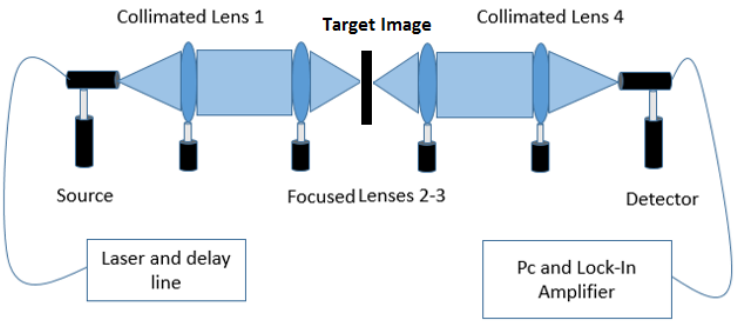

Figure 1.7: Typical scheme of a TD-THz system with the presence of an object between THz emitter and THz receiver

THz Imaging is often used to investigate a wide range of materials of interest for civil (industrial) applications, that they are often named ”dual use”. T-waves properties, in fact, allow detecting and locating millimetric and submillimetric defects present in specific samples. This can be exploited for (i) inline monitoring of industrial processes and quality control of the final products; (ii) investigation of damage caused by aging, due to intensive use or to external factors as impacts, real delaminations, artificial inserts, water contamination, (iii) identification of hidden elements behind concrete walls or other obstacles.

As an example of ”dual use” application, one can mention the analysis and detection of defects that can be achieved using T-waves on industrial composites, such as those based on Kevlar, fiberglass and carbon fibers. These materials, thanks to their robustness and lightness, are highly used for the realization of airplanes, cars, flak jackets and other products where early damage detection is extremely important in order to guarantee safety [31].

1.2 Eddy Current testing

Eddy Current Testing (ECT) is a Non Destructive technique widely used in many industrial application fields in which it is very important to detect the presence of thin defects (generally called cracks) in conductive materials. Features of this technique are the cost-effective implementation and the kind of retrieved measured data that make possible to estimate the geometrical characteristics of a crack as position, length, width and depth. The analysis of these characteristics allows the user to accept or discard realized components then improving the production chain [26],[32], [33]. Even if the physical principle that lies upstream of the ECT technique is very simple, its use for crack characterization purpose (i.e. evaluation of the geometric characteristics of the cracks) rather than for the only crack detection is a key issue in literature. In fact, many aspects have to be taken into account and suitably optimized during the overall measurement process. They mainly concern the realization of suitable measurement setup and post processing stages [34]. With respect to the measurement setup, the choice and the performance of measurement and excitation devices are of utmost importance. As for the former aspect, in the last years the literature have deeply explored physical principles and manufacturing techniques with the aim of realizing very good eddy current sensors and probes. Technologies as those based on coils, fluxgate, fluxset, Giant Magneto Resistance (GMR), hall effect and so on, have been analysed and adopted to realize ECT instruments. [33], [34]. Recent studies are involved in finding excitation solutions able to promote the measurement process. In this scenario, a key ingredient of the measurement process is the choice of signal type, frequency and amplitude to be adopted in the excitation stage. The criticality consists in finding excitation signals capable of causing sufficient amplitudes of eddy currents both for defects present on the surface of the material and for defects included in the material [2], [33].

For this reasons, *Betta et. al.* in rif. [33] have developed and analyzed two different ECT excitation strategies, that concern with the use of multifrequency and chirp signals.

1.2.1 Probe GMR description and basics of ECT

In ECT techniques a variable magnetic field $B_{ext}(t)$ is generated by a coil or an electro-magnet placed near the surface of the Sample-Under-Inspection (SUT). Under this excitation, the SUT reacts by producing a secondary magnetic field $B_{eddy}(t)$ for the presence of eddy currents in it. By applying proper

measurement strategies, this secondary field can be measured with high accuracy. Two main approaches have been used so far in ECT applications: the first one in chronological order makes use of a coil to pick up the variations due to the secondary field by measuring its flux over the coil (quite often is the same excitation coil that is used also as receiver and its impedance variation is measured), the second one employs magnetic field sensors such as Hall or Giant Magneto Resistance (GMR) probes to directly measure the total magnetic field $B_{ext}(t) + B_{eddy}(t)$ in the proximity of the SUT surface. The ECT relies on the fact that for samples composed of an homogeneous conductive and not-ferromagnetic material, as the Aluminum here considered, if edge effects can be disregarded, $B_{eddy}(t)$ does not change if the electromagnet is simply translated over the SUT; on the contrary, when the electromagnet is moved over a region of the SUT in which there is a discontinuity, an inclusion or a void, the spatial distribution of the eddy currents changes and, as a consequence, the secondary magnetic field changes too. By analyzing the variation $\Delta B_{eddy}(t)$ of the secondary field due to a defect (that can be a discontinuity, a void, a crack, and so on), some information about the nature and the geometric characteristics of the inhomogeneity can be inferred, such as the depth with respect to the inspection surface, the equivalent volume, the electrical conductivity, etc. [1], [26].

The probe is a Giant Magneto Resistance (GMR) sensor, used for eddy-current nondestructive testing on conductive materials. Today, on the market, different technologies are presented and are adopted in the realization of the probe. Among them, the GMR seems well suited for the purpose due to their large signal level, physical size, high sensitivity, low power consumption and low cost. Thanks to field-dependent changes in resistance that is possible to be observe in thin-film ferromagnetic/nonmagnetic metallic multilayers it is possible to know the operation method of GMR, in fact, in the absence of an applied field, GMR sensitivity shows a high value due to the scattering between oppositely polarized electrons in the antiferro magnetically coupled multilayers of the device. To reduce the GMR sensitivity, eliminating the scattering mechanism, an external field is applied and this aligns the magnetic moments of the ferromagnetic layers. The main objective of this activity is to realize a crack characterization and estimate both the crack depth and height. Authors Betta and Ferrigno has also developed a characteristics of the considered GMR sensor that is reported in [1].

Finally, The GMR-based ECT probe is composed by the previously selected GMR sensor, a permanent magnet, an exciting coil, and a signal con-

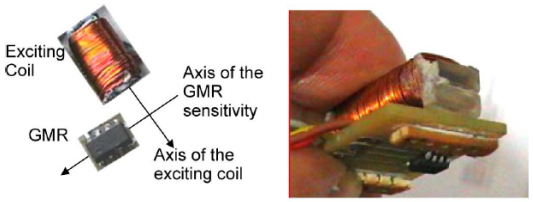

Figure 1.8: (a) Schematic and photo of the arrangement of the exciting coil and the GMR sensor [1]

ditioning system. The signal conditioning system is composed of a suitable instrumentation amplifier (Analog Devices AD620) with a fixed gain equal to 10. The permanent magnet is adopted to fix the dc bias in the GMR characteristics. As far as the exciting coil, it is realized with 288 turns and has a total dimension of $22mmx10mmx1.6mm$. In Fig. 1.8 sketches schematic pictures of the realized prototypal ECT probe with a detail of the arrangement of the exciting coil and the GMR sensor are shown.

1.2.2 Multi-Frequency Signal

Generally, a multifrequency signal is realized combining some sinusoidal tones in order to excite the desired frequency components with the desired amplitudes. The general formulation of a multi-sine signal is given in eq. 1.9 [2]:

$$I(t) = \sum_{k=1}^{N_s} I_k * \sin(2 * \pi * f_k * t + \phi_k) \tag{1.9}$$

where I_k is the current amplitude of the $k-th$ sinusoidal, f_k and ϕ_k are respectively the frequency and the phase of the $k-th$ sinusoidal and N_s is the number of considered tones. With a proper choice of ϕ_k:

$$\phi_k = -\pi * \frac{k(k-1)}{N_s} \tag{1.10}$$

the resulting excitation exhibits a quite constant envelope, which is desirable for optimizing the power delivered to the exciting probe. In Fig. 1.9 an example of multifrequency signal composed of 20 tones up to 10 kHz and with equal amplitudes.

In addition, it is evident to notice that the higher the number of tones the better are the information retrieved from the eddy currents on the specimen.

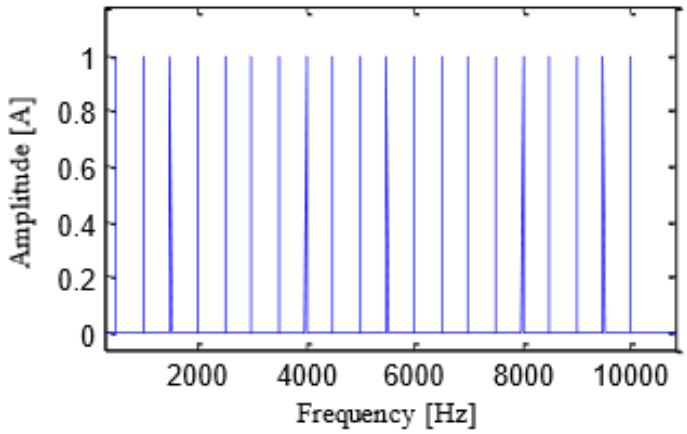

Figure 1.9: Example of a multisine signal considering 20 sinusoidal tones [2]

On the other hand, the higher the number of tones, the higher the total root mean square value of the generated signal. If this value is too high, problems related to the excitation coil heating and the power supply dimensioning arise. For these reasons generally a finite number of tones is suitably chosen. Useful considerations concerning with the relationships between the adopted frequencies and the specimen depth might drive the choice of tone number, frequencies and amplitudes [2], [33].

1.2.3 Chirp Signal

By tuning the amplitudes I_k and the phases ϕ_k, multi-tone signals can be generated in order to follow an arbitrary power spectrum while minimizing the peak factor, as said. In the case of N_s different harmonically related frequencies with constant power for each tone, the phases ϕ_k are derived from the continuous phase function of linear frequency modulated signals, i.e. from a Linear Chirp signal [2], [33], [35]. The Linear Chirp signal is one of the most used waveform used in pulse compression applications such as radar, sonar, spread spectrum communications, etc. and it is described by the general expression in eq. 1.11

$$s(t) = \alpha(t) \sin(\Phi(t)) \tag{1.11}$$

where

$$\Phi(t) = 2\pi\left(f_1 t + \frac{f_2 - f_1}{2T}t^2\right) \tag{1.12}$$

is a quadratic phase term ensuring a linear varying instantaneous frequency $f_i(t) = \frac{1}{2\pi}\frac{d\Phi}{dt} = f_1 + \frac{f_2 - f_1}{T}t$. $\alpha(t)$ is a windowing function that is not-vanishing only in the interval $[0, T]$. More generally, $\alpha(t)$ can be used to modulates the amplitude of $s(t)$ and, due to the characteristic of linear chirp, also the power spectrum. An example of chirp signal is shown in Fig. 1.10.

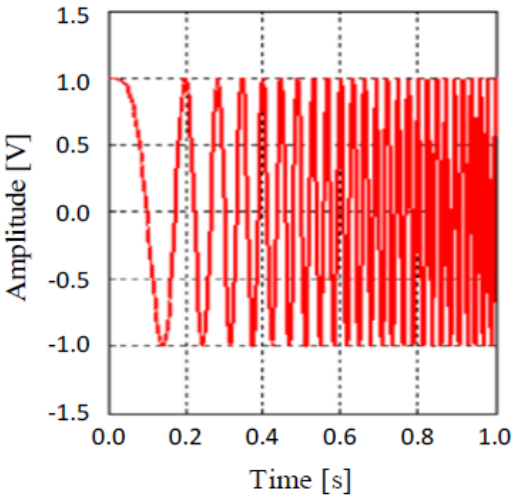

Figure 1.10: Time behaviour of a linear chirp. [2]

By replacing the multitone signal with a chirp one, a continuous frequency range can be excited providing potentially a better resolution in evaluating the more sensitive inspection frequency for a given defect. Nevertheless, also the number of tones can be increased in the multitone signal to guarantee the wanted resolution so that the main advantage of the chirp excitation actually does not lie in its continuous frequency range of excitation but indeed is represented by the possibility to characterize contextually the time and the frequenc domain response of the sample. In particular, besides of reconstructing the transfer function $H(\omega)$ in the frequency range of interest, the impulse response $h(t)$ of the sample can be retrieved by using a pulse-compression procedure. Since it was found that time and frequency analysis can provide complementary information about defects and moreover they are differently

affected by the possible noise sources (environmental, lift-off variation, etc), the contextual analysis can improve the defect detection capability. [2], [26], [33].

Finally, the two approaches are quite similar, there are some differences and it is interesting to establish which technique provides better performances. In particular, while Chirp assures a higher information content than multi-tone, for both the continuous frequency range of excitation and the possibility to reconstruct also the impulse response, the multitone signal reduces significantly the complexity of data processing and also concentrates the energy in a discrete number of frequencies then assuring a high SNR for these values. At the same time the chirp signal, similarly to the Pulsed Eddy Current, allows the excitation of very low frequencies also for short signal duration.

1.3 Fundamentals of Compressive Sampling

The Shannon-Nyquist sampling theorem states that it is possible to sample at least two times faster than the signal bandwidth to prevent harmful information loss when capturing a signal [36]. In many applications, including digital image and video cameras, the required Nyquist rate is so high that too many samples are acquired, making compression a necessity before storing or transmitting operations. In other applications, including imaging systems (medical scanners and radars) and high-speed analog-to-digital converters, increasing the sampling rate is very expensive. Recently a novel sensing/sampling paradigm, known as Compressive Sampling (CS), that goes against the common wisdom in data acquisition has been proposed [37]. Compressive Sampling theory asserts that it is possible to recover certain signals and images from far fewer samples or measurements than traditional methods use [38], [39]. In other words, the new method is able to capture and represent compressible signals at a rate significantly below the Nyquist rate. A CS technique can be divided in two fundamental stages: (i) a first step in which the input signal is directly acquired in a compressed form; (ii) a second step in which the output signal is correctly reconstructed by means application of opportune CS-Solver. [40].

To make this possible, CS relies on two principles: sparsity, which pertains to the signals of interest, and incoherence, which pertains to the sensing modality.

- *Sparsity* expresses the idea that the "information rate" of a continuous time signal may be much smaller than suggested by its bandwidth, or

that a discrete-time signal depends on a number of degrees of freedom which is comparably much smaller than its (finite) length. More precisely, CS exploits the fact that many natural signals are sparse or compressible in the sense that they have concise representations when expressed in the proper basis Ψ [41];

- *Incoherence* extends the duality between time and frequency and expresses the idea that objects having a sparse representation in Ψ must be spread out in the domain in which they are acquired, just as a Dirac or a spike in the time domain is spread out in the frequency domain. Put differently, incoherence says that unlike the signal of interest, the sampling/sensing waveforms have an extremely dense representation in Ψ [42].

The crucial observation is that it is possible to design efficient sensing or sampling protocols that capture the useful information content embedded in a sparse signal and condense it into a small amount of data [43]. These protocols are non adaptive and simply require correlating the signal with a small number of fixed waveform that are incoherent with the sparsifying basis. What is most remarkable about these sampling protocols is that they allow a sensor to capture very efficiently the information in a sparse signal without trying to comprehend that signal. Further, there is a way to use numerical optimization to reconstruct the full-length signal from the small amount of collected data.

Compressive Sampling affirms that an image or a signal can be reconstructed with a number of samples lower than that required by the traditional method of sampling, if there is an orthonormal basis $\Psi \in R^{NxN}$, where the signal can be represented through only few coefficients significantly different from zero [38]. So considering the NxN matrix $[\Psi_1|\Psi_2|...|\Psi_N]$, with the vectors $\{\Psi_i\}$ as the columns, the signal **x** can be expressed as:

$$\mathbf{x} = \sum_{i=1}^{N} f_i * \Psi_i \tag{1.13}$$

or

$$\mathbf{x} = \Psi\ \mathbf{f} \tag{1.14}$$

where **f** is the Nx1 column vector of coefficients, obtained as inner product of signal **x** and the matrix NxN: $f_i = \langle x, \Psi \rangle = (\Psi_i)^T x$. For the sake of clarity, **x** and **f** rappresent the same signal, **x** in space or time domain while **f** in Ψ

domain. In this case, the signal **x** is said to be *K-sparse*, in fact it is a linear combination of only *K* basis vectors, so only *K* of the coefficients in the 1.14 are nonzero and $(N - K)$ are zero.

In the truth, CS allows to take an unknown image of *N* pixels to reconstruct it with a much smaller number of measurements, for example *M*, than the number of pixels in the image. So that, considering the signal **x** and a collection of vectors $\{\phi_j\}_{j=1}^{M}$ $M \ll N$, it is possible to determine and consider another linear combination process that consists in $M \ll N$ inner product between the signal and the collection of vector. These products determine a new vector of measurements, in which each element is $y_j = \langle x, \phi_j \rangle$. Now, each element y_j can be arranged in a vector of $Mx1$ elements, and it is possible to define the measurements vectors ϕ_j^T as rows of a matrix MxN, so called matrix Φ. In this way, the sequence of measurements $\mathbf{y} \in R^m$ and the input signal $\mathbf{x} \in R^n$ can be expressed by the fundamental expression of CS theory:

$$\mathbf{y} = \Phi x \tag{1.15}$$

where $\mathbf{x} \in R^{Nx1}$ is the the unknown image to be reconstructed, in particular an ordered vector of pixels, that is obtained reshaping the pixel matrix of the image into a single column; $\mathbf{y} \in R^{Mx1}$ is the measurements vector, and $\Phi \in R^{MxN}$ is a matrix called sampling matrix that models the process of acquisition, and allows to select M values from which the reconstruction of the original signal starts. [9].

The system described by eq. 1.15 determins an undeterminated system of linear equations; it is said to be ill-posed and this system presents infinite solutions, so that there are infinite possible reconstructed signals $\hat{\mathbf{x}}$. Considering the assumption that the signal **x** is represented with $K - sparse$ coefficients in an apportune basis, the vector of measurements can be expressed combinationing eq. 1.14 and eq. 1.15 as:

$$\mathbf{y = \Phi x = \Phi \Psi\ f} \tag{1.16}$$

Introducing a new MxN matrix, called sensing matrix, and indicated as $A \in R^{MxN} = \Phi\Psi$, the eq. 1.16 can be express as:

$$\mathbf{y = Af} \tag{1.17}$$

Once again, the system is undeterminated, but the sparsity of **f** can be exploited to find an appropriate solution, in fact it is possible to recover **x** by solving an optimization problem, as shown in the following:

$$\hat{\mathbf{f}} = \arg\min_{f} ||\mathbf{f}||_1 \quad s.t \quad \mathbf{f} \in \mathbf{B(y)} \tag{1.18}$$

where $||.||_1$ represents the $l_1 - norm$, while the consistence with the samples **y** is represented by **B(y)**. After having estimate the solution $\hat{\mathbf{f}}$, the input signal of interest can easily be recovered by means of eq. 1.13

$$\hat{\mathbf{x}} = \Psi\hat{\mathbf{f}} \tag{1.19}$$

Finally, it is possible to consider also the minimum number of samples or measurements, and the require for a reliable reconstruction of image x is provided by following equation:

$$M \geq C * \mu^2(\Phi, \Psi) * \log(N) \tag{1.20}$$

where *C* is a certain positive constant, *K* is the sparsity of the signal of interest , *N* is the total number of pixels that have to be reconstructed and $\mu^2(\Phi, \Psi)$ is the so-called *coherence* between the sampling matrix Φ and the transformation matrix Ψ, that provides the maximum correlation between the two matrices, and that is expressed in eq. 1.21. The greater its value, the greater the number of samples required for a reliable reconstruction of k-sparse vector, so with the aim of strongly reducing the number of measurements to be taken, a low value of coherence it is necessary. The coherence is defines as:

$$\mu(\Phi, \Psi) = \sqrt{n} \max_{1 \leq k,j \leq n} | < \varphi_k, \psi_j > | \tag{1.21}$$

where φ_k and ψ_j are $k - th$ row and $j - th$ column of the matrices Φ and Ψ.

As stated in [39], in order to reconstruct reliably the sparse signal, the coherence between the sampling matrix Φ and the transformation matrix Ψ has to be minimized. Fortunately, in many cases of practical interest, choosing a random matrix as sampling matrix Φ assures a low value of coherence to be obtained with a wide set of orthonormal basis Φ. The sampling matrix Φ is usually realized as a random sequence of entries set to 1 or 0 otherwise, with equal probability.

Considering that the measurement number is lower than the pixel number image, the eq.1.20 represents a ill-poses system where the number of unknown elements is greater than the number of equations and generally, it has a infinite number of solutions. For this, there are some different solvers that give the possibility of inverting the problem realizing operations of minimization. Examples of these solvers [44], [45] are: *L1-Magic*, *CVX*, *TVAL3* and others

where each ones can be applied in consideration to particular cases. The authors adopted the *Total Variation (TVAL3)* [46], [47] algorithm built by means of a combination of the classic augmented Lagrangian method with an appropriate variable splitting and non-monotone alternating direction method for sub-problems [48]. In fact, the purpose of variable splitting is to separate the non-differentiable part in order to easily find its closed form solution while applying the general *TVAL3* algorithm. The main advantage of the general *TVAL3* method is its low computational cost, since it requires only two or three matrix-vector multiplications to process one inner iteration.

Chapter 2

Proposed Methods

2.1 Shielding Effectiveness of NTC

The huge increase of high-frequency electronic systems and telecommunication devices has raised the pollution due to electromagnetic (EM) signals to a level never seen before. Electro Magnetic Interference (EMI) is the adverse effect caused by EM waves emitted by electrical circuits on the performance of devices operating nearby at a similar frequency range or on surrounding living/biological species. The quest for novel materials with high efficiency to mitigate EMI has become a mainstream field of research, motivated not only by environmental issues but also by a large variety of applications. Broadly speaking, EMI shielding is defined as the prevention or reduction of the propagation of electric and magnetic waves from one region to another by using conducting or magnetic materials. The shielding reduces coupling between signals, cross-talk among electrical components, noise in cables and communication systems, etc. At radio and microwave frequencies, EMI is regulated by legal requirements that electronic devices must satisfy in order to operate properly and avoid affecting the performance of other equipments. With the increasing speed of electronic circuits, Terahertz (THz) EMI shielding is becoming progressively more important [2]. Effective attenuation solutions are required in many THz circuits systems, where not much research has been performed to date. As a matter of fact, since research in this elusive frequency range is still in its infancy, at the moment no regulations, certified measurements, or even reference standards on EMI shielding exist. Furthermore, shielding in the terahertz region may have applications in homeland security and defense to protect information acquired by imaging and

sensing techniques or personnel involved in ground operations, e.g. in airport body scanners or in the spectral detection of CBRN (Chemical, Biological, Radiological and Nuclear) materials. Finally, a high EMI shielding effectiveness (SE) is the basis for the development of high performance and low-cost THz quasi-optical components, such as polarizers and mesh filters, that can be widely exploited in spectroscopy, interferometry, imaging and sensing, among other areas. The SE of a system is governed by three processes, namely, reflection, absorption, and multiple internal reflection and it depends upon various parameters such as conductivity, permittivity, permeability, and thickness of the constituent materials, with most of these factors being cross-linked to each other. EMI shielding effectiveness (SE) is expressed in decibel (dB) and it corresponds to the ratio between field strength with and without the presence of a protective medium. In general, a shielding range of 10 to 30 dB provides the lowest effective level of shielding, while anything below that range can be considered little or no shielding. Shielding between 60 and 90 dB may be considered a high level of protection, while 90 to 120 dB is exceptional. A shielding effectiveness of 30 dB, corresponding to 99.9 % attenuation of the EMI radiation, is considered as an adequate level of shielding for many applications [49], [50]. Sometimes, it is assumed that the shielding level from the composite is ultimately the same as the conductivity of an isotropic metal [51].

Presently, the most common way to shield electrical circuits is by reflection owing to the use of metallic sheets. When using a metal with a very high relative permeability, a similar shielding mechanism is obtained for the magnetic field at relatively low frequency. However, EMI shielding with metals has a number of drawbacks limiting a broad applicability, primarily the poor mechanical flexibility due to the high stiffness and weight density, cost, propensity to corrosion, and limited tuning of the shielding effectiveness. Moreover, the electromagnetic pollution is not truly eliminated, but only mitigated since the electromagnetic signals are almost completely reflected at the exterior of the metallic shields.

In the last years, a number of experiments have been focused on the design and fabrication of systems where EM shielding is primarily based on the absorption of polymer based materials because of their lightness, low cost, easy shaping, and biocompatibility [52]. Since most polymers possess intrinsic electrical insulating properties making them poorly opaque to electromagnetic waves, conductive and/or magnetic nanoparticles have been dispersed in appropriate concentrations in order to dissipate the radiation power and to limit at the same time the total reflection occurring at the surface. Composite materials

containing carbon-based fillers, like nanotubes both single-walled (*SWCNT*) and multi-walled (*MWCNT*), nanofibers, onion-like carbons, nanowhiskers, have shown good EMI shielding effectiveness in the THz frequency domain, mainly owning to their electro-conductive properties [53]. Furthermore, these materials show additional unique properties (e.g. chemical inertness, water repellence and self-cleaning ability) making them good candidates for cost-effective manufacturing of functionally flexible THz quasi-optical components [54]. When considered for coatings or in thin film form, carbon nanocomposites can be easily patterned using established methods, such as inkjet-printing, thus bypassing the complex photolithography and etching processes required for making conventional THz quasi-optical devices and components [55].

The shielding properties of *SWNT*- and *MWNT*- polymeric composites have been studied extensively at frequencies ranging from 10 MHz to several GHz using network analyzer systems [56], The study of the EMI shielding properties of polymeric composites loaded with carbon nanotubes is becoming increasingly important nowadays in the THz frequency range, because of the ever-increasing speed of electronic devices.

THz Time Domain Spectroscopy (THz-TDS) is a well-established technique which allows measuring the complex-valued dielectric parameters of the materials in the THz spectral range (typically 0.1-3 THz) [57], [58]. As both amplitude and phase spectra are simultaneously unraveled in THz-TDS, the real and imaginary part of the dielectric parameters such as permittivity, refractive index and conductivity of the materials can be inferred without using Kramers-Kronig relations. Further, THz-TDS is an all-optical, and hence noninvasive, technique, which is particularly suitable for probing intra-band transitions such as, free carrier and low-energy phonon excitations, as THz radiation features weak photon energy and low field amplitude [59] − [61] .

The transmission function $\hat{T}$ of a dielectric slab with a complex-valued refractive index $\hat{n} = n - ik$ and thickness d is related to the ratio between the Fourier transformed THz signals transmitted respectively through the sample $\hat{E}_{sam}$ and through the air $\hat{E}_{ref}$ by:

$$\hat{T}(\omega) = \frac{4\hat{n}}{(\hat{n}+1)^2} * \exp\left[-\frac{i(\hat{n}+1)\omega d}{c}\right] * \hat{FP}(\omega) = \frac{\hat{E}_{sam}(\omega)}{\hat{E}_{ref}(\omega)} \quad (2.1)$$

where c is the speed of light in vacuum, ω is the angular frequency and $\hat{FP}(\omega)$ is the Fabry-Perot term accounting for multiple internal reflections inside the sample to the eq. 1.4, so that the complex valued refractive index of the material of interest can be retrieved by numerically solving eq. 2.1 and 1.4 as

discussed for instance in the references [18], [62].

In terms of shielding effectiveness $SE(\omega) = -20log|\hat{T}(\omega)|$ equation 2.1 can be rewritten as:

$$SE(\omega) = 20\log\left(|\frac{(\hat{n}+1)^2}{4\hat{n}}|\right) + 20\log(e)\frac{\alpha d}{2} + 20\log\left(|\hat{FP}^{-1}|\right) = SE_R + SE_A + SE_{FP} \tag{2.2}$$

where $\alpha = \frac{2\omega k}{c}$ is the absorption coefficient of the sample. In eq. 2.2 the different contributions to the shielding effectiveness are intentionally highlighted. Losses due to the direct absorption inside the material SE_A, and those arising from direct or multiple internal reflections from the sample, respectively SE_R and SE_{FP} can be distinguished and separately quantified in THz-TDS. It should be noted that the last term in eq. 2.2 a) it gives an oscillatory behavior to the SE and b) it is the only that can negatively contribute to the SE. However, if the thickness of the slab is much larger than the inverse of the lowest THz wavenumber, as in the case of our experiments, multiple internal reflections can be safely ignored.

2.2 Eddy Current Testing with CS

The Eddy Current Testing sometimes has been applied to a very big area of interest and it could be characterized by presence or not of defect and cracks. These defects are sometimes collocated in the center of the sample under test, a GMR schematic and investigation area are shown in Fig. 2.1. This investigated area can be considered as a matrix of NxN pixels, where of each pixel two different signals, current and voltage, are acquired with a huge number of samples, about 100000. This means that memory data are needed to be very big, and time reconstruction is too long because the knowing of all the signal is requested. The purpose of CS in ECT is to reduce the memory size, reducing the number of samples acquired for each signal, and limit the reconstruction time to a few seconds. So that, it has been focused on the best estimate value of the reconstruction samples, and on determine the CS-algorithm/CS-Solver that permits to reduce reconstruction time. Also, to reduce acquisition and reconstruction times, CS has been combined with some particular graphics solutions as *Compute Unified Device Architecture*, so-called $(CUDA)$ and *Graphic Processing Unit*, (GPU).

In order to realize a detailed analysis, the study of has seen the applications of two different CS-Solver: the basic *Matching Pursuit*, indicated with *MP*,

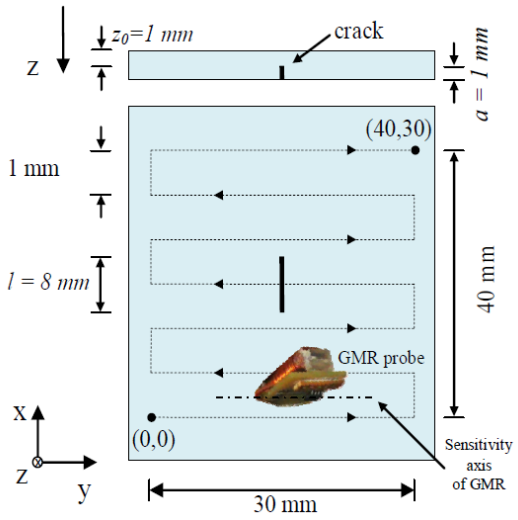

Figure 2.1: (a)Sketch of the orthogonal scan for a specimen with sub superficial crack.

and the evoluted *Compressive Sampling Matching Pursuit*, so-called CoSaMP. Both these solvers have been applied with specific parameters criteria, that will be shown in the following sections.

Matching Pursuit Algorithm

MP is a particular class of iterative algorithms that gives the possibility to decompose a signal into a linear expansion of functions in order to form a dictionary. This algorithm was introduced for the first time by Mallat and Zhang [63]. Basically, the main idea of MP is that at each iteration of the algorithm, it chooses dictionary elements in a greedy fashion that best approximate the signal. Considering a Hilbert space, $\mathcal{H}$, and a dictionary, called also family of vectors, D = $\{\mathfrak{g}_\gamma\}_{\gamma\in\Gamma}$ where, $||\mathfrak{g}_\gamma|| = 1$ it is possible to let a closed linear span of the dictionary, $\mathbb{V}$ and to affirm that the dictionary is complete if and only if $\mathbb{V} = \mathcal{H}$. Inside the Hilbert space a function $\mathfrak{f}$ is considered, that is enlarged linearly over the dictionary D by successive approximation. In fact for any vector $\mathfrak{g} \in D$, $\mathfrak{f}$ could be decompose as following:

$$\mathfrak{f} =< \mathfrak{f}, \mathfrak{g} > \mathfrak{g} + \mathfrak{r}^{(\mathfrak{g})} \tag{2.3}$$

where $\mathfrak{r}^{(\mathfrak{g})}$ is the residual after approximating $\mathfrak{f}$ by $\mathfrak{g}$, and as the residual is

orthogonal to $\mathfrak{f}$, it is possible to estimate the norm of the residual and so of $\mathfrak{f}$, in fact:

$$||\mathfrak{f}||^2 = |<\mathfrak{f}, \mathfrak{g}>|^2 \mathfrak{g} + ||\mathfrak{r}^{(\mathfrak{g})}||^2 \tag{2.4}$$

The residual is a parameter that it is possible to study applying the algorithm in fact the "best" approximation is obtained when the norm of the residual is minimum, and so maximize $|<\mathfrak{f}, \mathfrak{g}>|^2$.

At each iteration of the matching pursuit algorithm it is necessary to choose the almost best approximation for the current residual from the dictionary. Considering *n* interactions, $n-th$ order residual $\mathfrak{r}^{(n)}$ is necessary. The almost best function $\mathfrak{g}^{(n+1)}$ is chosen from D and $\mathfrak{r}^{(n)}$ is decomposing into:

$$\mathfrak{r}^{(n)} =< \mathfrak{r}^{(n)}, \mathfrak{g}^{(n)} > \mathfrak{g}^{(n)} + \mathfrak{r}^{(n+1)} \tag{2.5}$$

Now, this decomposition is applied also to the original function $\mathfrak{f}$ as so:

$$\mathfrak{f} = \sum_{i=0}^{n} < \mathfrak{r}^{(i)}, \mathfrak{g}^{(i)} > \mathfrak{g}^{(i)} + \mathfrak{r}^{(i+1)} \tag{2.6}$$

Because the residual $\mathfrak{r}^{(i+1)}$ is always orthogonal to $\mathfrak{r}^{(i)}$ it is possible to say:

$$||\mathfrak{f}||^2 = \sum_{i=0}^{n} |<\mathfrak{f}, \mathfrak{g}^{(i)}>|^2 + ||\mathfrak{r}^{(i+1)}||^2 \tag{2.7}$$

However, other algorithms based on MP are possible to consider, in fact Orthogonal Matching Pursuit (OMP) is an improvement of the first one. The main idea is the same of MP, in fact at every iteration an element is taken form the dictionary that best approximates the residual. In this algorithm the original function is fit to all the already selected dictionary elements via least squares or projecting orthogonally onto all selected dictionary atoms, rather than taking the scalar product of the residual and the new dictionary element to get the coefficient weight.

Compressive Sampling Matching Pursuit Algorithm

The CoSaMP (COmpressive SAmpling Matching Pursuit) algorithm is an extension of Orthogonal Matching Pursuit, published for the first time in a Needell and Tropp's paper [64], [65]. The basic idea of the algorithm is the same of OMP [66], but COSaMP has tighter bounds on its convergence and performance. Nevertheless it is important to notice that the CoSaMP algorithm requires, as input, four pieces of information:

1. Have access to the sampling operator via matrix or vector multiplication;

2. Define a samples' vector (noise) of the unknown signal;

3. Know the sparsity of the approximation to be realized;

4. A stop criterion.

Then, it consists of five main steps, where each of them is linked to a particular lemma analyzing its performance.

1. *Identification*: it is necessary to find the largest 2s component of the signal proxy;

2. *Support Merge*: The support of the signal proxy merges with the support of the solution from the previous iteration;

3. *Estimation*: A solution via least square is estimated with the constraint that the solution accepts a particular support;

4. *Pruning*: The estimated solution is taken and compressed to the required support;

5. *Sample Update*: The "sample" is updated, taking into account the residual.

These steps are considered in the following script of CoSaMP algorithm:

These steps are repeated until the stop criterion (a halting criterion) is triggered, a possible example is to consider as criterion a fixed number of iterations.

2.2.1 Sampling instant determination

According to the CS theory, Φ is a random sampling matrix characterized by m rows and n columns. As for the entries of the matrix, for each row only one element is different from zero and equal to one. A suitable procedure, based on a standard random number generator, has been adopted to set the column of

Input:

- s the sparsity of $\mathbf{x}$
- $\mathbf{y} \in \mathbb{R}^m$ and the measurement matrix $\Phi \in \mathbb{R}^{m \times n}$

Output:

- $\hat{\mathbf{x}} \in \mathbb{R}^n$ such that $\hat{\mathbf{x}}$ is s-sparse and $\mathbf{y} = \Phi\hat{\mathbf{x}}$

1: $\mathbf{x}^{(0)} \leftarrow \mathbf{0}$
2: $\mathbf{v} \leftarrow \mathbf{y}$
3: $k \leftarrow 0$
4: **while** Halting condition false **do**
5: $\quad k \leftarrow k+1$
6: $\quad \mathbf{z} \leftarrow \Phi^{\mathsf{T}}\mathbf{v}$ ▷ Signal proxy
7: $\quad \Omega \leftarrow \text{supp}\left(\mathbf{z}^{2s}\right)$ ▷ Support of best $2s$-sparse approximation "Identification"
8: $\quad \Gamma \leftarrow \Omega \cup \text{supp}\left(\mathbf{x}^{(k-1)}\right)$ ▷ Merge supports
9: $\quad \bar{\mathbf{x}} \leftarrow \arg\min_{\tilde{\mathbf{x}}:\text{supp}(\tilde{\mathbf{x}})=\Gamma} \|\Phi\tilde{\mathbf{x}} - \mathbf{y}\|_2$ ▷ Solve Least Squares
10: $\quad \mathbf{x}^{(k)} \leftarrow \bar{\mathbf{x}}^s$ ▷ Prune: best s-sparse approximation
11: $\quad \mathbf{v} \leftarrow \mathbf{y} - \Phi\mathbf{x}^{(k)}$ ▷ Update current sample
12: **end while**
13: $\hat{\mathbf{x}} \leftarrow \mathbf{x}^{(k)}$
14: **return** $\hat{\mathbf{x}}$

Figure 2.2: CoSaMP algorithm steps

the non-null entries. For the sake of the clarity, let us suppose to have a matrix with 3 rows and 5 columns [67]:

$$\Phi = \begin{bmatrix} 1 & 0 & 0 & 0 & 0 \\ 0 & 1 & 0 & 0 & 0 \\ 0 & 0 & 0 & 0 & 1 \end{bmatrix} \tag{2.8}$$

If an input signal x is sampling according to what stated in eq. 1.15 with a particular matrix that permits to take into account eq. 1.17

$$\begin{bmatrix} y(0) \\ y(1) \\ y(2) \end{bmatrix} = \begin{bmatrix} 1 & 0 & 0 & 0 & 0 \\ 0 & 1 & 0 & 0 & 0 \\ 0 & 0 & 0 & 0 & 1 \end{bmatrix} * \begin{bmatrix} x(0) \\ x(1) \\ x(2) \\ x(3) \\ x(4) \end{bmatrix} = \begin{bmatrix} x(0) \\ x(1) \\ x(4) \end{bmatrix} \tag{2.9}$$

i.e. y turns out to be a random sampled version of the input signal whose index corresponds to the column of Φ with non-null entries. As for the trans-

formation matrix Ψ, it is set according to Fourier basis as following:

$$\Psi = \begin{bmatrix} \Psi_{0,0} & \Psi_{0,1} & \Psi_{0,2} & \Psi_{0,3} & \Psi_{0,4} \\ \Psi_{1,0} & \Psi_{1,1} & \Psi_{1,2} & \Psi_{1,3} & \Psi_{1,4} \\ \Psi_{2,0} & \Psi_{2,1} & \Psi_{2,2} & \Psi_{2,3} & \Psi_{2,4} \\ \Psi_{3,0} & \Psi_{3,1} & \Psi_{3,2} & \Psi_{3,3} & \Psi_{3,4} \\ \Psi_{4,0} & \Psi_{4,1} & \Psi_{4,2} & \Psi_{4,3} & \Psi_{4,4} \end{bmatrix} \tag{2.10}$$

The *A* matrix can be determined by applying the relation 1.16

$$A = \begin{bmatrix} \Psi_{0,0} & \Psi_{0,1} & \Psi_{0,2} & \Psi_{0,3} & \Psi_{0,4} \\ \Psi_{1,0} & \Psi_{1,1} & \Psi_{1,2} & \Psi_{1,3} & \Psi_{1,4} \\ \Psi_{4,0} & \Psi_{4,1} & \Psi_{4,2} & \Psi_{4,3} & \Psi_{4,4} \end{bmatrix} \tag{2.11}$$

As it can be appreciated, thanks to the suitable choice of the sampling matrix, the matrix *A* turns out to be a sub-matrix of Ψ; this way, the computational burden of the method is reduced since the matrix *A* is not calculated from an actual multiplication, but it is evaluated as the rows of the transformation matrix whose index is equal to that of the sampling instant.

2.3 Compressive sampling approach for THz-based non-invasive tests

To suitably apply the CS approach to THz Imaging [68], two main modifications have to be brought to the THz systems shown in Fig. 1.7 , i.e. (*i*) defining a suitable sampling strategy and (*ii*) adjusting correspondingly the characteristics of the THz beam.
As regards the sampling strategy, the random sampling matrix is realized by means of a set of M random masks. Each mask is modeled as a two-dimensional matrix, composed by N pixels having random features of transmitting or blocking the THz radiation, with equal probability. With regard to the beam characteristics, in RS technique the THz radiation is focused on a single point (pixel) of the target. On the contrary, in CS-based THz systems, the THz beam is collimated on the whole area to be analyzed as shown in Fig. 2.3b. A real picture of the above system described is shown in Fig. 2.3c.

As a consequence, the THz radiation detected at the receiver, is the superposition of beam portions passed through the each pixel of a random mask. The entry of the measurement vector $\mathbf{y}$ associated with each mask is then obtained

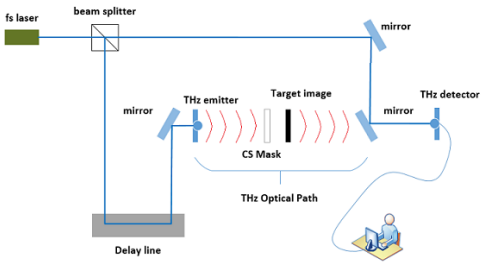

(a)

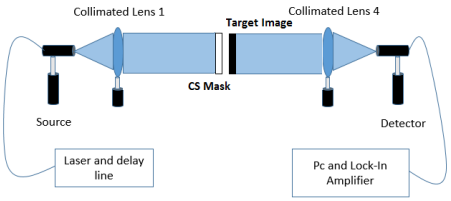

(b)

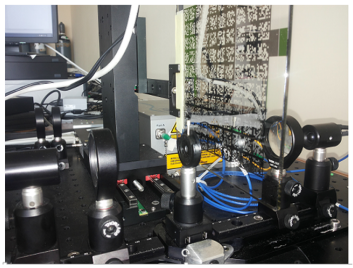

(c)

Figure 2.3: (a) CS-based approach applied to THz Imaging systems, obtained with a suitable set of masks inserted between the beam source and the target; (b) Collimated configuration of THz system; (c) real CS-THz system.

from the snapshot of the THz field acquired at the receiver in time-domain.
In order to reduce the duration of the Imaging process, the set of M masks can be assembled on a single board, which is moved by a dual-axis linear stepper motor. The board position with respect to the beam is, thus, modified $M \ll N$ times, while the target is fixed during all the acquisition stage, with a corresponding, significant reduction of total capture time. From a mathematical point of view, the corresponding implementation of $\mathbf{\Phi}$ is shown in Fig. 2.4, where each one of the M masks has been reshaped into a single row of N pixels of the sampling matrix. According to the transparency of each pixel of the mask, the entries of each row of the sampling matrix $\mathbf{\Phi}$ are set equal either to 1, if the corresponding pixel transmits the THz radiation, or 0 otherwise. Consequentially, the sampling matrix $\mathbf{\Phi}(M,N)$, involving M rows and N columns, is obtained.

In conclusion, Raster Scan gives the possibility of Imaging the desired tar-

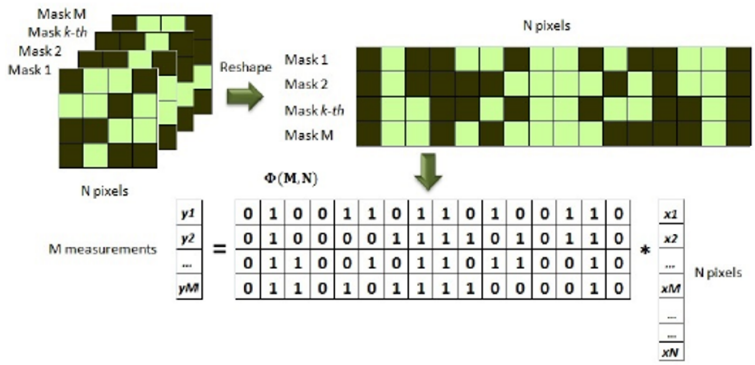

Figure 2.4: Implementation of the sampling matrix $\mathbf{\Phi}$ with random masks.

Table 2.1: Comparison between RS and CS-based THz Imaging in terms of acquisition interval (t), pixel resolution (r), and number of measurements (n).

Property	Raster Scan(RS)	Compressive Sampling(CS)
t	Could be very long	Very fast
n	All area of interest	Limited number of masks
r	Very good	Similar to RS

get with an excellent resolution, which directly affects the time acquisition, since each pixel of the final image has to be measured (Tab.2.1). On the contrary, CS-THz Imaging takes advantage from the underlying CS framework to reduce strongly the number of required measurement (only M masks are needed), granting a final resolution similar to that of RS-based Imaging. The main difference consists of a degradation of the overall quality of the reconstructed image that can be theoretically limited increasing the number of considered masks.

2.3.1 Uncertainty sources in CS-THZ Imaging system

In Fig. 2.5 the scheme of CS-THz Imaging measurement is shown, where each block models an operating step of the measurement process. Five main blocks can be recognized: (i) THz Emitter, that generates the beam; (ii) THz Receiver, that provides the signal associated with the radiation that passed through the sample under test; (iii) CS Reconstruction, where the received THz signal is manipulated according to (1.15) in order to estimate the reconstructed image;

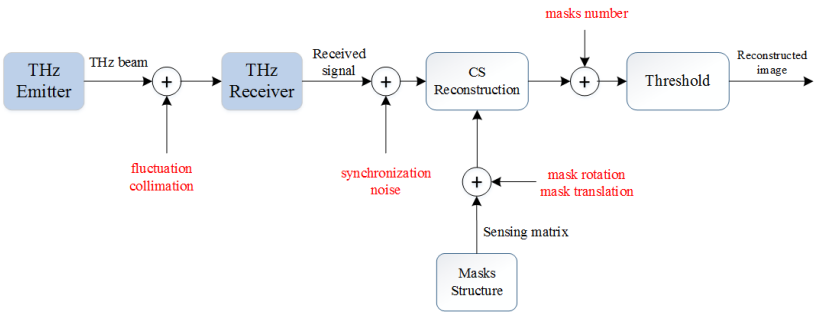

Figure 2.5: Scheme of CS-THz Imaging measurement process.

(iv) Mask Structure, that provides the sensing matrix as explained in Fig. 2.4; and (v) Threshold, where, with the aim of denoising the reconstructed image, the grey pixels are forced to be black or white.
The figure, moreover, highlights in red the uncertainty sources characterizing each operating step, that afflict the related output. As regards the THz system, researches on the uncertainty source and their effect on the THz image measurements are already available in literature [69], [70]. On the contrary, the literature is lacking as concerns the uncertainty associated with the CS-based approach. Authors, then, have focused their attention on the uncertainty affecting the CS reconstruction and its impact on the overall quality of the reconstructed image. In the following, the main uncertainty sources introduced by the application of CS approach are discussed.

2.3.2 Number of masks

CS fundamentals provide information about the minimum number of masks to be used in order to reliably reconstruct the image of interest. However, the output of the reconstruction algorithm is an estimate whose accuracy is strictly dependent on the number of available measurements.
In principle, if all the other uncertainty sources are neglected and all the components of the measurement station are supposed to be ideal, it is easy to observe that the higher the number of masks, the lower the uncertainty affecting the reconstructed image. However, in actual measurement set up, this assumption could not be verified.

2.3.3 Mask-target misalignment

Another uncertainty source considered for the performance assessment of CS-based THz Imaging systems is the masks-target alignment; in particular, two quantities have been taken into account for the alignment assessment, i.e. rotation and translation of masks in the vertical plane with respect to the target. Considered factors are, in fact, the most important issues in alignment process and affect the quality of reconstructed images also in the presence of their very limited values. As shown below, their final effect on the reconstructed image consists of a more shades of gray.

2.3.4 Threshold level

Since the masks exhibit a random distribution of pixels, in correspondence of the defect, only some masks allow the THz radiation to reach receiver, while the others will block the beam. However, pixels of reconstructed image appear usually in shades of grey and not only white or black, particularly when the alignment between masks and target is not precise. It is often useful, thus, to apply a threshold on pixels values; if the value exceeds the threshold, it is forced to 1, otherwise to 0. As a consequence, the reconstructed image is directly and highly dependent on the threshold value adopted. As an example, in Fig.2.6 the resulting images after having applied threshold respectively of 90 %, 70 % and 50 % of the maximum value (i.e. intensity) of reconstructed pixels, are shown.

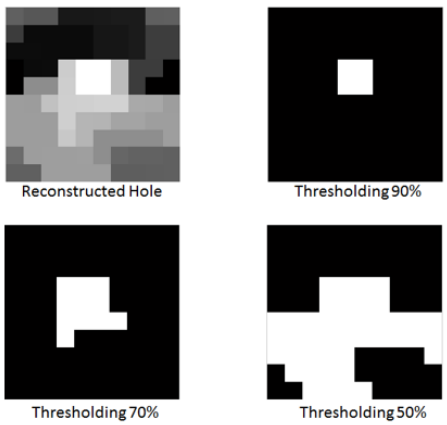

Figure 2.6: Reconstructed square hole of 2x2 mm^2 with 16 measurements and with different threshold values

Chapter 3

Results

3.1 TDS-THz System CeSMA

During the research project, all the experimental tests dealt and developed for THz technology have been developed using a Time Domain Spectroscopy (TDS) THz system provided by the German manufacturer of MenloSystem, which has installed and realized the initial setup. A diagram of the system is shown in the Fig. 3.1, followed by the real measurement system. In figure, the main components are indicated with a letter/character presented in the following list:

a. T-Light/FS Laser

b. ODU box: taht contains an electromagnetic delay line;

c. Optical Lenses;

d. Source PCA;

e. Detector PCA;

f. Lock-In Amplifier.

A schematic representation of the optical setup is shown in Fig. 3.1. The T-Light femtosecond fiber laser presents two fiber-coupled outputs, port *A* and *B*. The fiber coupled terahertz emitter antenna (*Tera15-SL25-FC*) is connected to the output port A directly via a 1m fiber patch cord. The input fiber from the optical delay unit (ODU) is connected to port B of the femtosecond fiber laser.

The ODU's output fiber port is connected to the detector antenna (*Tera15-DP25-FC*) using a mating sleeve. The Terahertz radiation is guided from the emitter antenna Tx to the detector antenna Rx through four polymer lenses (lens 1 to lens 4). The lenses have an effective focal length of approximately $EFL = 54$ mm and a working distance of WD = 46 mm. The silicon lens of the emitter antenna and *lens 1* collimate the divergent terahertz radiation to a parallel terahertz radiation beam. The silicon lens of the detector antenna and *lens 4* project the radiation onto the detector antenna. *Lens 2* and *lens 3* generate an intermediate focal point, as shown in Fig. 3.2a. The system can also be operated with a collimated THz-beam (without *lens 2* and *lens 3* inside the optical path), as shown in Fig. 3.2b. Removing the lenses will result in a different temporal pulse position and might require some adjustment of the THz pulse. The THz radiation generated by the *Tera15-SL25-FC* antenna is linearly polarized, thus rotating the antenna may decrease the performance of the spectrometer.

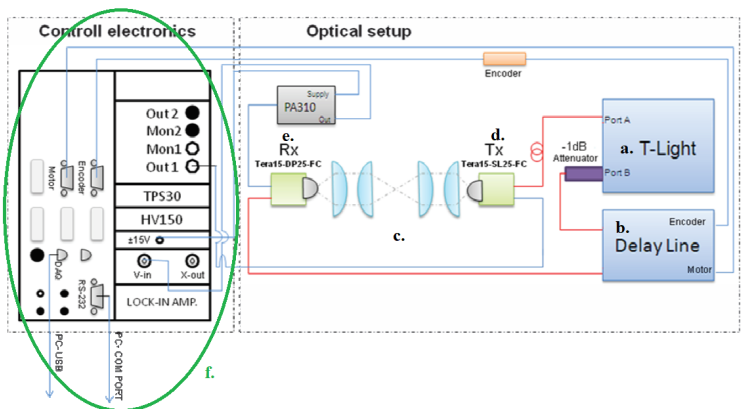

Figure 3.1: Architecture of THz-TDS Menlo System

Characteristics and properties of THz system used in the research project are reported in the table 3.1. For more informations and properties about THz components, it is possible to consult the different manuals and data sheets, in the following tables, some informations about the different components are reported.

THz System	
Model	TERA K15 - Menlo System
Laser	T-Light-III-F9
Spectral Range	$> 3.0\ THz$
Dynamic Range	$> 60\ dB$
Scaning Range	$< 5\ GHz$
Antenna bias	$0... \pm 20\ V$
Modulation frequwncy	$100Hz < f < 100kHz$
Supply netvoltage	$110/230\ V$
THz Emitter	
Antenna Type	Tera15-TX-FC
Bias, V	Unipolar, 0-60 V
Waveform	Sine
Frequency $[kHz]$	70 - 100
Optical Power $[mW]$	37
Central Wavelength $[nm]$	1550
Laser rep. rate	80 MHz to 250 MHz
THz Detector	
Antenna Type	Tera15-RX-FC
Optical Power $[mW]$	34.1
Central Wavelength $[nm]$	1550
Laser rep. rate	80 MHz to 250 MHz
Max Dc Voltage $[V]$	2
Lock-In Amp.	
Time constant $[ms]$	100
Sensitivity $[mV]$	30
Suppley Voltage $[V]$	$\pm$22
Signal-Input-Voltage DC $[V]$	$\pm$70
Signal-Input-Voltage AC $[V_{pp}]$	$\pm$ 50
Ref-Input-Voltage $[V]$	$\pm$ 15
Logic-Inputs $[V]$	-5...+15

Table 3.1: Properties of the THz components that costitued THz system used in the research project.

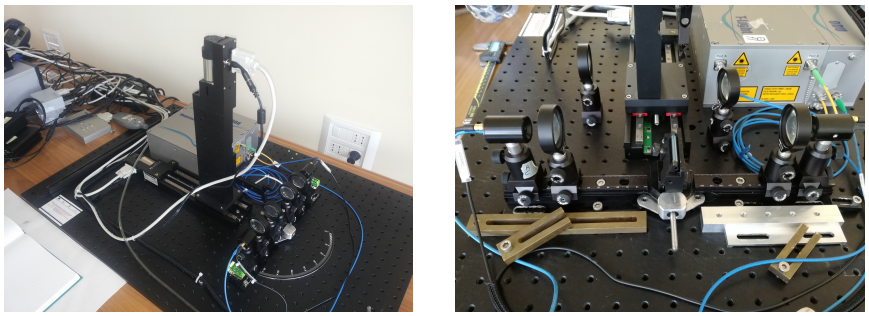

(a) (b)

Figure 3.2: Example of THz-TDS system in (a.) trasmission focalized and (b.) trasmission collimated.

3.1.1 Characterization System

Before to present the different results obtained in the different topics previous presented, it is necessary to present the results of the study and measurement of THz beam. This operation is very useful and important especially to understand which is the minimum resolution value to appreciate a small sample under investigation. For the sake of the clarity, the evaluation of THz beam has been realize on the THz-TDS system with a focused configuration, because this is the limit case that could be considered. First of all, it is noticed that the femtosecond laser allows to realize a Gaussian beam and therefore a distribution like the one shown in the Fig. 3.3.

The most appropriate method to make THz beam analysis is to apply the Knife-Edge. This method evaluates the size of the THz beam starting from the knowledge of its total intensity, obtained by evaluating the signal without inserting any sample under test. After inserting the sample into the support and moving it in a certain direction, it has been reached the 10% and 90% of the total intensity value. The spatial range that the stepper motor realizes from 10 % to 90 % correspond to the size of the beam in that particular direction [71], [72].

A sample piece of aluminum of "L" shape was inserted into the specimen port holder of the instrument and the influence of the sample on the beam distribution was analyzed by performing a displacement along the X axis and along the Y axis of the support. Along these axes, it is chosen to move the support of one millimeter at a time and to perform a deeper fitting if either of the two limit values 10% or 90% was exceeded abundantly. The movement

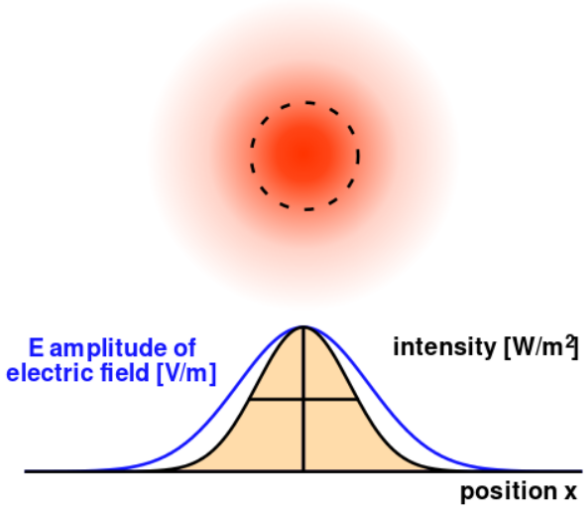

Figure 3.3: Typical trend of a Gaussian beam, where in the center the most of intensity is focused.

of the support was possible thanks to the use of the *C-863 Mercury Servo Controller*, even though it has been optimized using the internal program options made available by MenloSystem. The analysis along the X axis was performed by moving the sample inside the holder from one position x_0 to a position x_1, then to the right and from x_0 to x_2 on the left, while the analysis along the Y axis was performed by moving the sample inside the holder from a position y_0 to a position y_1, then to the top and from y_0 to y_2 on the bottom, as shown in the Fig. 3.4

The analysis has shown a THz beam's size equal to $2x2mm^2$ in a focalized configuration, and the trend of the beam in Fig. 3.5 are reported. A same analysis has also been realized when the THz system is in collimated configuration. In this case, the transition from focused configuration to collimated one has determined a broadening of THz beam, inasmuch the two lenses used for focusing the beam have been removed. THz beam size are $8x8mm^2$ and the particular trends of the beam in the Fig. 3.6 are reported.

In collimated configuration, THz beam has been studied also in reflection mode, in this case the strength of THz beam has been evaluated directly on the emitter and detector, results and trends in Fig. 3.7 are reported.

For the sake of the clarity, in the Fig. 3.14 all the possible configuration

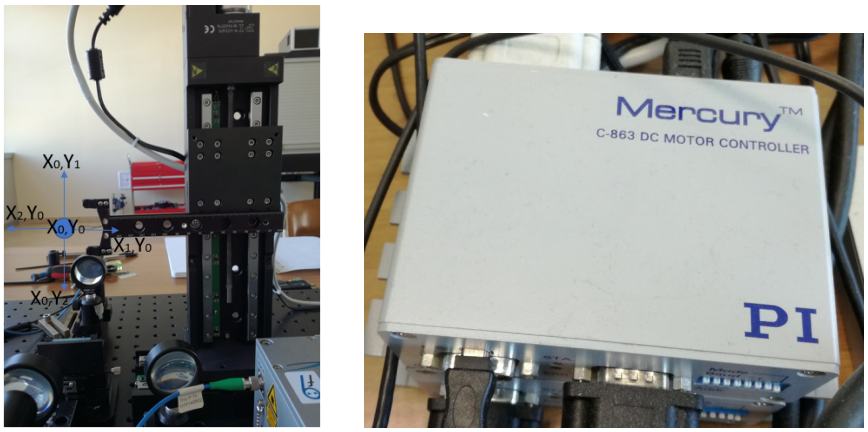

(a) (b)

Figure 3.4: (a) Stage *XY* in which the movimentation of it is shown; (b) stepper motor used to manage the stage *XY*

that THz system could employed are reported.

Finally, with the different configurations that the THz system could be assumed and they are shown in Fig. 3.14 and some THz Imaging acquisitions have been realized as shown in the Fig. 3.9.

3.2 Shielding Effectiveness of NTC-components

As first results, the study on matrices of commercial PBAT/PHBV blend with $70:30$ weight ratio, here simply coded as *ENMAT* are shown. They was supplied in pellet form from *Ningbo Tianan Biologic Material Co. Ltd.* (Tianan-ENMAT) (China) under the commercial name *6010P* and a polypropylene resin PP (*Monsten MA524*, $Mn = 32.400 g/mol$; $Mw = 250.084 g/mol$, melt flow index $24.0 g/10 min$ at 230°C, 2.16 kg) supplied by *UNIPETROL RPA*. Multi-walled carbon nanotubes used as fillers first biodegradable matrix differ essentially in terms of their aspect ratio parameter, as clearly highlighted in table 3.2.

As fillers of the synthetic PP, instead, three types of multi-wall carbon nanotubes, one neat, one chemically modified with carboxyl $-COOH$, and one modified with amino $-NH_2$ groups, supplied by *Nanocyl S.A. (Sambreville - Belgium)*, were used as fillers. The nanotubes have the same purity, length and aspect ratio. Raw materials (matrix and fillers) were always pre-dried at 70°C

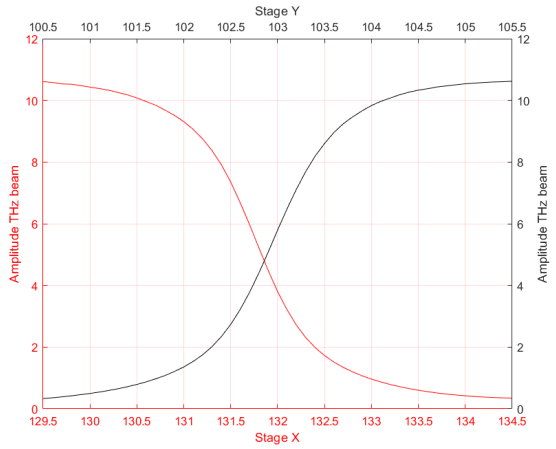

Figure 3.5: The trends of THz beam along the stage X (red) and Y (black) are reported, in particular on the two line the 10 % and 90 % of maximum intensity value of beam are indicated, so the calculation of diameter beam is immediated

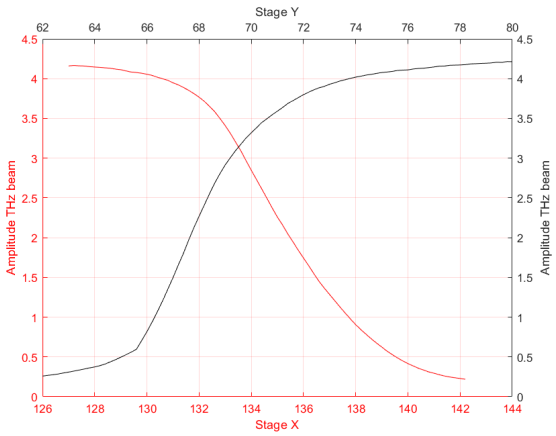

Figure 3.6: The trends of THz beam along the stage X (red) and Y (black) are reported, in particular on the two line the 10 % and 90 % of maximum intensity value of beam are indicated, so the calculation of diameter beam is immediate

for 12 hours under vacuum before melt compounding. Samples containing up to 1.2% in volume of each type of multi wall carbon nanotubes were then prepared using a *HAAKE Polylab* mixer at 175°C, with a screw speed of 60 rpm

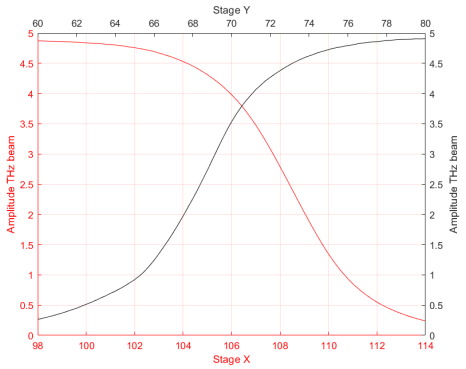

(a)

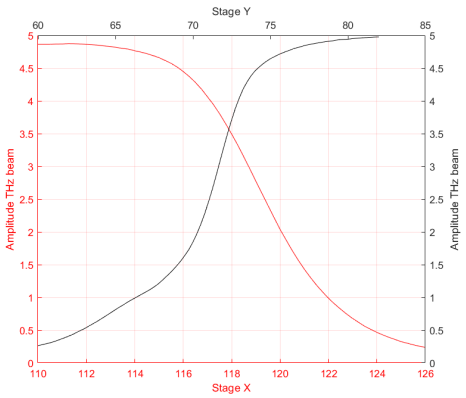

(b)

Figure 3.7: In order to study the strength of THz beam, in reflection modality, the beam size has been evaluated on the THz emitter (a), and also on THz detector (b.) The trends are very similar between them and the diameter value is $9x11mm^2$.

and a residence time of 7 min. The actual filler content, subsequently verified by thermogravimetric analyses, was always close to the nominal one. Samples of each system were prepared by compression molding with the help of a lab hydraulic press *(LabTech Engineering, LP20-B)* operating at $180°$C under the pressure of 2 MPa. Furthermore, these materials show additional unique properties (e.g. chemical inertness, water repellence and self-cleaning ability) making them good candidates for cost-effective manufacturing of functionally flexible THz quasi-optical components [54]. When considered for coatings or in thin film form, carbon nanocomposites can be easily patterned using es-

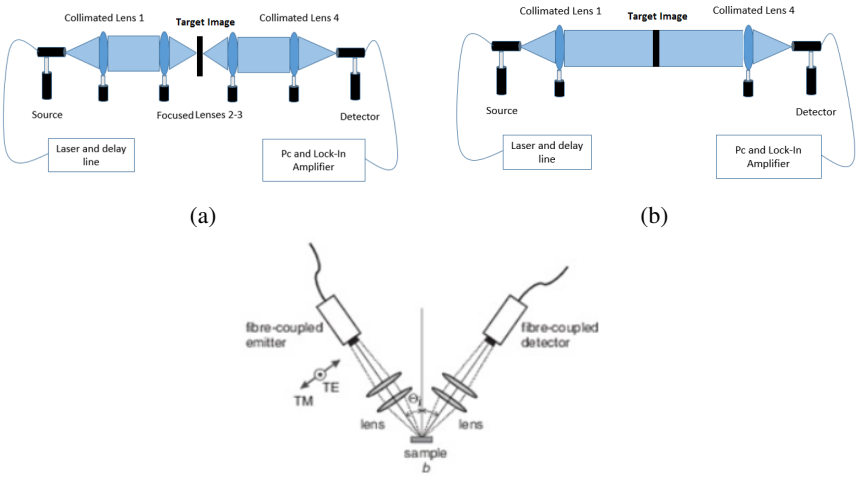

Figure 3.8: The two common configuration of a THz-TDS system: (a) focused; (b) collimated; (c) reflection mode.

tablished methods, such as inkjet-printing, thus bypassing the complex photolithography and etching processes required for making conventional THz quasi-optical devices and components [55].

In order of what has been presented in 2.1, the main contribution to the shielding effectiveness of our MWCNTs composites is given by the THz absorption in the bulk material (Fig. 3.10).

Reflections arising from the first air-sample interface and multiple internal reflections can be both neglected (insets of Fig. 3.10), a poor reflectivity and, simultaneously, high absorption coefficient at THz frequencies make these nanocomposites excellent materials for THz shielding applications. The THz absorption of MWCNTs composites strongly depends on the concentration of the filler: the higher the concentration of nanotubes, the higher the absorption because of an increased conductivity of the material which, in turn, can be attributed either to an improved mobility of the carriers or to a higher carrier density or to both factors. Surprisingly, MWCNTs featuring different aspect ratios such as those with $\eta = 30$ and $\eta = 667$ (Fig. 3.10a and 3.10c respectively) show comparable values of shielding effectiveness at the same concentrations of MWCNTs, despite their respective percolation thresholds [73] . On the contrary, the best performing samples in terms of shielding ef-

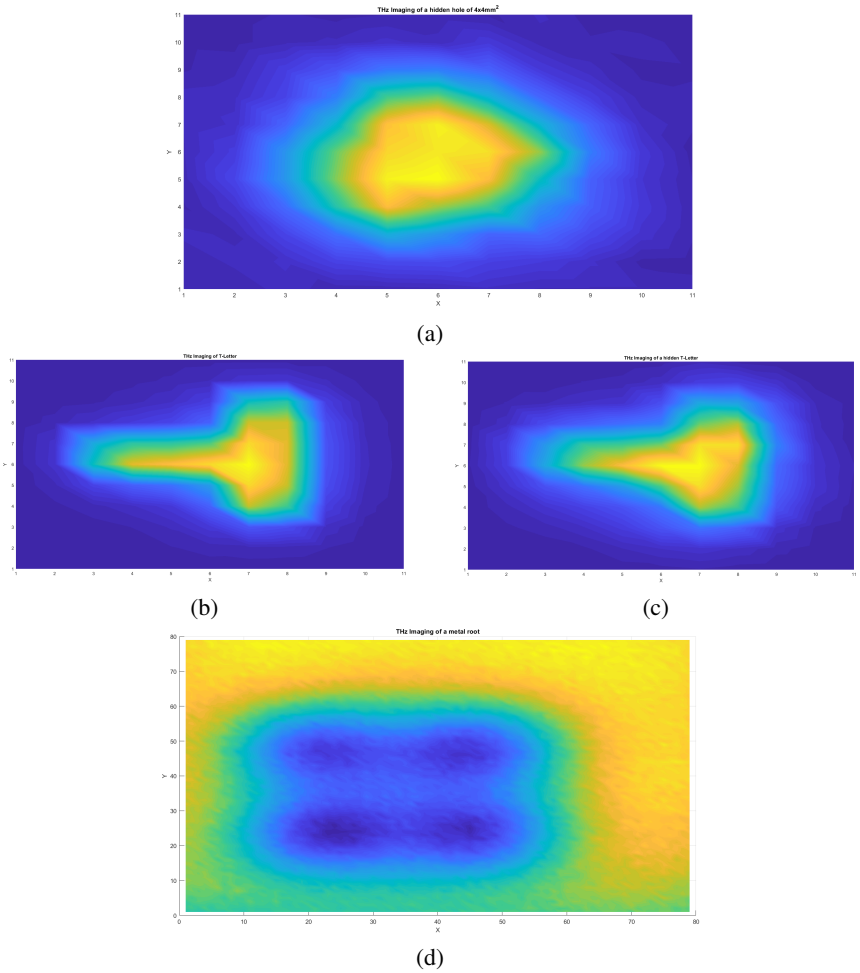

Figure 3.9: (a) Imaging of a hidden hole of $4x4mm^2$. The hole is hiddene inside a structure composed by two pieces of cement of few value thickness; (b) Imaging of T-letter; (c) Imaging of the same T-letter hidden by a piece of cement; (d) Imaging of a metal rood.

fectiveness are those with MWCNTs featuring an intermediate aspect ratio, η = 105. This result is in partial contradiction with the data trend reported in reference [74], where polymeric composites of SWCNTs show higher values of shielding effectiveness with increasing length but having the same diameter. However the diameters as well as the lengths of the MWCNTs employed in

Table 3.2: List and properties of multi-waller carbon nanotubes used in the study of THz-SE

Trade code	**Supplier**	**Mean outer diameter**	**Length (μm)**	**Aspect ratio [η]**	**True density (g/cc)**	**Purity (%)**
4060	*Shenzen Nanotechnologies*	50	1,5	30	2,16	$> 97\%$
3150	*Nanocyl*	9,5	1	105	1,94	$> 95\%$
724769	*Sigma Aldrich*	7,5	5	667	2.1	$> 95\%$

our nano-composites vary significantly. The presence of a trade-off in terms of shielding effectiveness between length and diameter of the MWCNTs is somewhat expected. Although composites of MWCNTs with high aspect ratio can form more easily an inter-MWCNT transport network, in turn, the presence of many disordered MWCNTs bundles could hinder the carrier transport along the MWCNTs and degrade the shielding effectiveness. Further, when the concentration of MWCNTs exceeds the percolation threshold, the shielding effectiveness (thus the conductivity) of our MWCNTs composites does not change as dramatically as shown in our previous DC measurements [73]. Argue we can thus that the dielectric response of these composites at THz frequencies is dominated by the charge separation inside the MWCNTs leading to localized plasmonic resonances rather than by carrier transport through percolated pathways. This conclusion is in agreement with other THz measurements on single and multiwalled carbon nanotubes where the THz conductivity peak has been observed and attributed to plasmonic resonance [75], [76]. The aspect ratio of the MWCNTs is not the only parameter that can be tuned when designing MWCNTs composites for THz electromagnetic screening applications. The functionalization of the MWCNTs also plays an important role for the shielding effectiveness in MWCNTs composites. In Fig. 3.11 it is shown the shielding effectiveness of unfunctionalized and functionalized MWCNTs with COOH and NH_2 groups respectively, at same volume concentrations. Unfunctionalized MWCNTs feature higher absorption than the functionalized ones (Fig. 3.11). The absorption of THz radiation in MWCNTs composites depends not only on the concentration of MWCNTs but, obviously, on the polymeric matrix too. For example our PBAT/PHBV blend features a relatively high absorption coefficient compared to polypropylene (Fig. 3.11b)

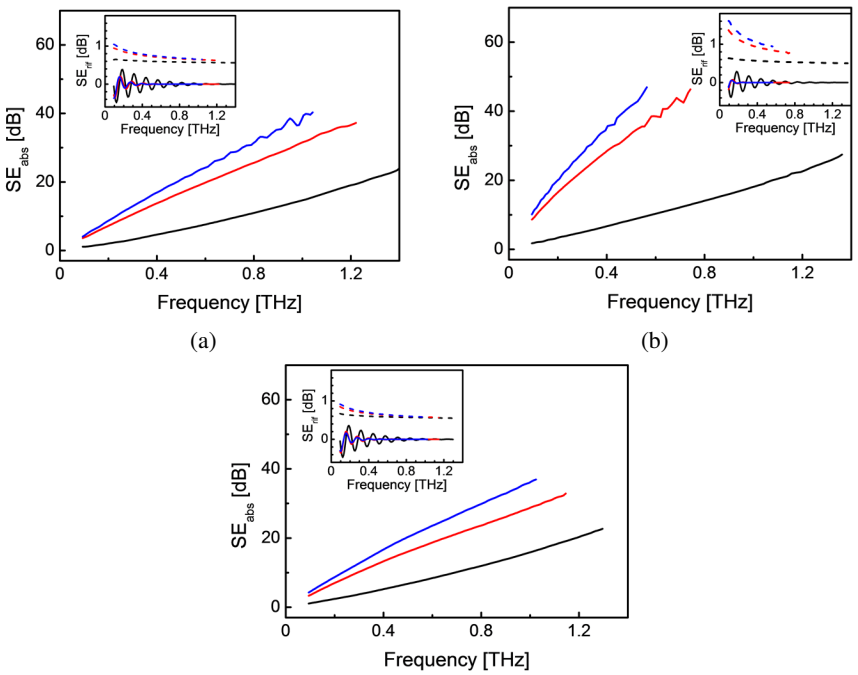

Figure 3.10: Main contribution to the shielding effectiveness due to the THz absorption in a *PBAT/PHBV* blend filled with *MWCNTs* featuring different volume concentrations, 0.1%, 0.7% and 1%, respectively black, red and blue curves and aspect ratios, 30, 105 and 667, respectively, (a), (b) and (c). Insets: Negligible contributions to the shielding effectiveness arising from direct and multiple internal reflections from the corresponding *MWCNTs* composites

3.3 Eddy Current Testing with CS

As explained in the CS introduction, an appropriate sensing matrix is necessary to realize the operation of reconstruction. In this case, sensing matrix's realization is developed creating two different sequences, in which the distinction has been made by considering a fixed and a variable sequence. This difference has been placed in order to evaluate some aspects, in fact with the fixed sequence it is possible to study the reproducibility of reconstruction process from the point of view of time by varying several factors, such as PCs, development environment, etc., while with the variable sequence it is possible to analyze the

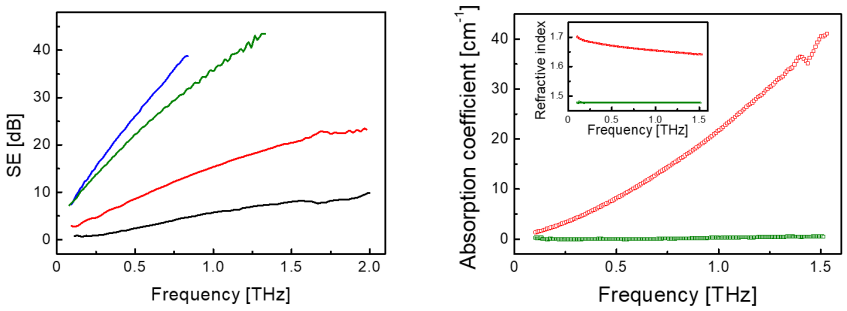

(a) (b)

Figure 3.11: (a) Shielding effectiveness of MWCNTs composites in a polypropylene matrix with MWCNTs functionalized with COOH and NH_2 groups, respectively black and red curves, and with unfunctionalized MWCNTs in, respectively, a polypropylene matrix (green curve) and a PBAT/PHBV blend (blue curve). Aspect ratio and volume concentration of MWCNTs are respectively 105 and 0.5%. (b) Absorption coefficient of the polypropylene and PBAT/PHBV matrix, respectively green and red curves and their corresponding refractive index (inset).

impact of the time on the sequence to reconstruct. Another important aspect is the length of the sequence. It is related to the number of samples that are used to carry out the reconstruction; so it means that given an signal with *n* samples, the reconstruction takes place of *m* samples, with *m* smaller than *n*, so that CS has reason to be applied.

The creation of the sequence is realized by a Matlab-script and it is generated in a random manner with *n* samples, where of these *n* samples for the fixed sequence is considered a slot of *m* samples, firmly fixed, which can be in the queue, in the head or in the middle of the sequence, while in the case of variable sequence, several successive slots of *m* samples are considered, as shown in Fig. 3.12.

The reconstruction process is realized on two specific signals, in particular they are electrical signals, current signal that responses to the excitation supplied in input and the GMR's voltage output. These two physical quantities are very important because some different method will be applied on them and with them it is possible realized the transfer's matrix where some important parameters of analysis are extracted. On current and voltage signal, CS approach is applied, in order to determine the necessary minimum number of samples, called *m*, useful to reconstructed the original signal acquired with a number of

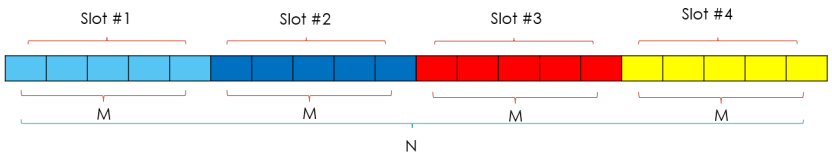

Figure 3.12: Representation of sequences considering for the sensing matrix realization, where *m* are the samples number used to reconstruct the signal, *Slot* are the portions of the complete sequence of *n* samples used to realize the sensing matrix.

samples equal to 100000, called *n*.
To find the best value of *m*, a parametric *m*-quantity is realized, and some different values are considered:

$$m = [200, 250, 300, 350, 400, 450, 500] \tag{3.1}$$

In this way, it is important to observe that for *m*-factor selection it necessary to respect the relation 1.20, in fact a little value of *m*-factor, for example 200 - 250, as also shown in the following figures, are not sufficient to reconstruct the original signal. While a higher value of *m*-factor is not necessary because authors are not interest in having a perfect reconstruction, that permits to have a matching between original and reconstructed signal, but they want to know approximately the *m*-factor value, that is more or less 300-400 according to the type of CS-method/solver applied, as shown in Fig. 3.13.

After that *m*-factor value is established, study has been developed the analysis considering the different CS solvers and the two different sequences in order to study time performances, all thanks to application of script file realized with Matlab software. In particular, more attention is focused on studying how much time is necessary to reconstruct the signal considering the different type of sequence and how big are the dimensions of signal that are transferred. Time's value obtained are not excessive, on the contrary values are contained to values under 5 seconds, in general, but with particular parameters' combinations more little values are possible, for example a half of second. Very little time values for reconstruction process are possible because in study it has been possible to consider processes/tools that permits the parallelization of operations, in fact it has been useful using *CUDA* and *GPU* operations.

During the simulation campaign another important parameter has been considered. First of all iterations number, called *iter*, that permits to verify when stopped the algorithms, and this is considered in particular for MP algo-

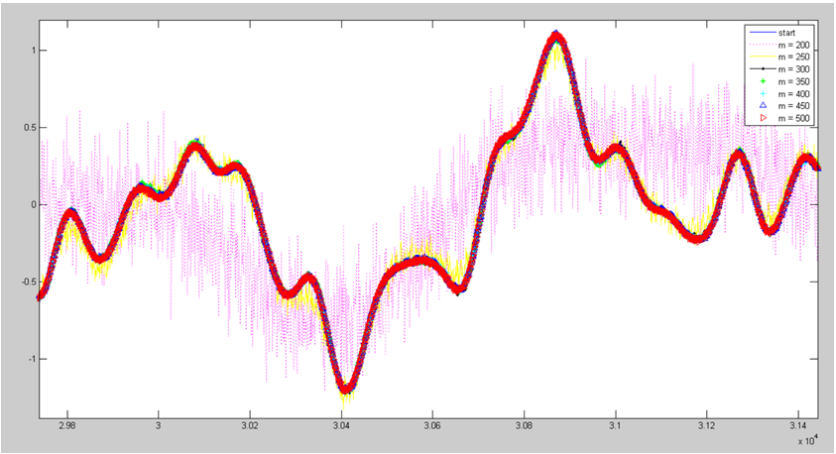

Figure 3.13: Zoom of current signal reconstruction obtained with the parametrization of *m*-parameter.

rithm, and tones or frequencies number, called *s*, that is the number of tones used to excite samples under test. The setting of *s*-parameter is possible only in the case of CoSaMP algorithm because in MP the determination of tones number is implicited.

In the following some tables are reported, in particular they show the necessary temporal values to reconstruct signals with MP and CoSaMP algorithm's taking account the changing of the parameters*m*, *iter*, and *s*, table 3.3, 3.4.

Table 3.3: Time reconstruction vs matrix sequences considering MP algorithm.

***m*-samples/iter**	**Fixed Seq** **50 — 75 — 100 — 125**	**Variable Seq** **50 — 75 — 100 — 125**
200	0.6 — 0.943 — 1.307 — 1.702	0.609 — 0.964 — 1.369 — 1.772
250	0.709 — 1.101 — 1.528 — 1.988	0.719 — 1.132 — 1.577 — 2.063
300	0.815 — 1.265 — 1.754 — 2.276	0.827 — 1.299 — 1.820 — 2.368
350	0.945 — 1.425 — 1.969 — 2.543	0.939 — 1.457 — 2.018 — 2.603
400	1.035 — 1.599 — 2.199 — 2.832	1.040 — 1.612 — 2.211 — 2.851
450	1.144 — 1.764 — 2.418 — 3.106	1.148 — 1.770 — 2.425 — 3.115
500	1.257 — 1.933 — 2.645 — 3.394	1.257 — 1.938 — 2.663 — 3.420

Table 3.4: Time reconstruction vs matrix sequences considering CoSaMP algorithm.

***m*-samples/tones**	**Fixed Seq** **30 — 40 — 50**	**Variable Seq** **30 — 40 — 50**
200	0.496 — 0.775 — 11.197	5.354 — 12.053 — 33.340
250	0.306 — 1.243 — 3.369	15.163 — 8.399 — 24.133
300	0.294 — 1.045 — 1.311	17.441 — 3.333 — 17.180
350	0.597 — 1.925 — 3.598	43.296 — 2.369 — 13.810
400	0.666 — 1.795 — 3.795	48.130 — 2.343 — 8.095
450	0.736 — 1.289 — 3.139	48.524 — 2.251 — 5.064

About the temporal analysis, it can be seen that time reconstruction values are very fast for both the algorithms, in fact with MP one the maximum value is about 1.3 s for m = 500, but in this case it is sufficient an m = 300 - 350 where the time values pass to 1.0 s, while with CoSaMP algorithm, time values has a significant decrease in fact the considerable value is 0.6 s. These results refer to a fixed sequence, while for a variable sequence, in the case of CoSaMP algorithm time values are lightly greater in fact it is preferable to use the MP algorithm where values with a variable sequence are comparable with the values obtained with a fixed sequence.

A same analysis has been developed to evaluate the error percentage of quality reconstruction, and results are shown in tables 3.5 and 3.6:

Table 3.5: Error percentage of quality reconstruction current signal considering MP algorithm and the two different matrix sequences.

***m*-samples/iter**	**Fixed Seq** **50 — 75 — 100 — 125**	**Variable Seq** **50 — 75 — 100 — 125**
200	96.94 — 97.98 — 98.24 — 98.32	90.24 — 91.29 — 91.61 — 91.70
250	22.59 — 23.85 — 24.29 — 24.43	23.43 — 17.37 — 17.52 — 17.75
300	9.08 — 4.38 — 4.62 — 4.75	13.65 — 6.32 — 5.84 — 6.08
350	10.46 — 4.48 — 4.43 — 4.64	11.73 — 5.07 — 4.80 — 5.03
400	7.96 — 4.17 — 4.44 — 4.57	10.75 — 4.66 — 4.45 — 4.67
450	9.60 — 4.16 — 4.26 — 4.43	9.98 — 4.38 — 4.25 — 4.45
500	9.69 — 4.19 — 4.19 — 4.37	9.50 — 4.20 — 4.14 — 4.33

In this case, significant results are obtained with CoSaMP algorithm, in

Table 3.6: Error percentage of quality reconstruction current signal considering CoSaMP algorithm and the two different matrix sequences.

***m*-samples/tones**	**Fixed Seq** **30 — 40 — 50**	**Variable Seq** **30 — 40 — 50**
200	84.53 — 103.63 — 126.08	77.27 — 88.05 — 100.71
250	27.42 — 4.26 — 4.43	29.59 — 11.55 — 21.17
300	27.36 — 3.85 — 4.27	27.44 — 3.99 — 4.36
350	27.36 — 3.74 — 4.09	27.37 — 3.87 — 4.17
400	28.13 — 3.61 — 3.88	27.34 — 3.75 — 4.04
450	27.36 — 3.64 — 3.79	27.35 — 3.68 — 3.94

fact it permits to the user to determine the tone numbers necessary in order to realize an acceptable reconstruction. In the particular case, both sequences are possible considering a tone number values equal to 40, taking in account of a bilateral spectrum, so in the truth only 20-tones are necessary, the error percentage is more or less of 4 $\%$.

In order to optimize all the reconstruction process, a graphic interface has been realized, in particular with the ausilium of a Matlab-script it has been possible create a GUI-Interface, in which it is possible to select and determine some inputs obtained some as output, the elements presented in the tables.

3.4 Compressive Sampling and THz

3.4.1 Sensitivity Analysis

In order to apply experimentally the CS theory, and in particular to have a real sensing matrix to apply the acquisition and reconstruction process, a set of M random masks has been realized by deposing a thin metallic film on a planar screen of quartz through a lithographic process realized by Toppan Photomasks, Inc.; screen dimensions are $6^{''} x 6^{''} x 0.250^{''}$, corresponding to 15.24x15.24x0.63 cm, capable of containing a number M of the masks equal to 100. Each mask is composed by 100 pixels, arranged in a matrix of 10x10 pixels; the pixels have equal probability of transmitting or blocking THz radiation and are characterized by a nominal dimension 1.0x1.0 mm^2.
In order to automatically generate the set of M masks, a suitable algorithm, written in Matlab^{TM} environment, has been implemented; different parameters (such as pixel dimension, distance between two adjacent masks, presence of

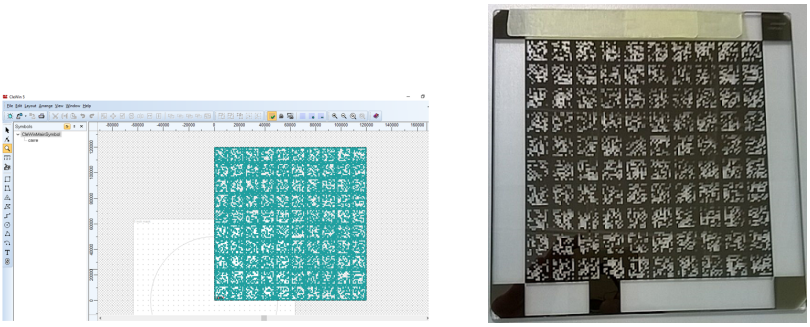

(a) (b)

Figure 3.14: (a) Realization of the masks in CleWin by PhoeniX Software; (b) Real set of random masks that compose the sensing matrix

a contour for each mask) were settable. The masks layout to be printed on a quartz planar screen has, then, been prepared in CleWin^{TM} by PhoeniX Software, one of the most important and utilized editor to produce physical layout for micro and nano-technology; as an example, Fig. 3.14a shows the layout of the masks set adopted in the successive experimental tests, while Fig. 3.14b shows the real mask implemented.

In order to assess the effect of the considered uncertainty sources on the final quality of the image reconstruction, a number of numerical tests has been carried out by means of an efficient design of experiments. In particular, tests aimed at estimating the evolution of the image quality versus the sources through a limited number of experimental runs have been carried out. The nominal image consists of 10x10 pixels background with a 2x2 pixels square hole. To enhance the estimates of the measured values, the resolution of both target and masks has been improved by a factor of 30 before executing rotation and translation operations. Furthermore, some numerical tests have been realized changing the pixel's sizes, but the analyses have shown similar results so only the above mentioned case is presented.

3.4.2 Image quality metrics

In order to assess the quality of an image reconstruction, a proper quality index has to be selected. In general, the approaches for image quality measurements can be classified in two main groups: *Pixel Difference Measurements* and *Human Visual Based Measurements*.[77] *Pixel Difference Measurements* estimate the quality of an image by performing the pixel-to-pixel difference between

the reconstructed image and the reference one. On the contrary, *Human Visual Based Measurements* exploits human perception as reference, taking into account parameters (such as brightness, contrast, texture or orientation) that can change the perceived quality of an image.
To compare the impact of the adopted metrics on the quality assessment, two indexes have been chosen, one for each considered approach. In particular, Mean Square Error (MSE) has been adopted as representative for *Pixel Difference Measurement* and Structural SIMilarity index ($SSIM$) for *Human Visual Based Measurement*, respectively. These are the most employed indexes in Full Reference (FR) image metrics, i.e. metrics of quality in which the reference image is fully available and, therefore, a *comprehensive* comparison between the reconstructed image and the reference image can be performed.[77],[78]
The MSE is defined as:

$$MSE = \frac{1}{KG}\sum_{i=1}^{K}\sum_{j=1}^{G}[X(i,j) - Y(i,j)]^2 \tag{3.2}$$

where K and G are, respectively, the number of pixel rows and columns of the images, $X\,(i,j)$ stands for the pixel value at the i-th row and j-th column of the reconstructed image, and $Y\,(i,j)$ represents the corresponding value of the reference image. The advantage characterizing the use of MSE are: (*i*) the limited computational burden, (*ii*) its similarity with other figure of merit usually adopted in signal theory and, therefore, characterized by clear meaning, and (*iii*) the interesting feature of satisfying the properties of convexity, and differentiability, so it can be used in optimization applications. Its main drawback is the independence on the image structure; as an example, two distorted images can have very different types of quality while having the same MSE.
The $SSIM$ is based on the hypothesis that the human eye perceives structural information of an image. This index, thus, measures the degradation of structural information, rather than the degradation of the quality of each pixel.
It is defined as:

$$SSIM = \frac{(2\mu_X\mu_Y + C_1)(2\sigma_{XY} + C_2)}{(\mu_X{}^2 + \mu_Y{}^2 + C_1)(\sigma_X{}^2 + \sigma_Y{}^2 + C_2)} \tag{3.3}$$

where σ_{XY} is the covariance of pixels of X and Y, and μ_X and $\sigma_X{}^2$ are, respectively, the pixels average and variance of the image X; the same quantities are defined also for the image Y. The two constants C_1 and C_2 are two very small values mandated to limit the $SSIM$ when the denominator approaches

zero; they are defined as $C_1=(K_1L)^2$ and $C_2=(K_2L)^2$, where L = 255 for 8-bit images, and $K_1K_2 \ll 1$[78]. The main advantage related to the use of $SSIM$ is the capability of estimating the degradation of the image structure as perceived by the human observer. The main drawback relies on the computational burden, that makes the $SSIM$ not suitable for real time application.
It is worth noting that the reference image *Y* has been numerically synthesized from the knowledge of the defect dimension expressed in pixels.

3.4.3 Central composite experimental design

To reduce the computational burden, an approach based on the Central Composite Design (CCD)[79] has been followed. The CCD, in fact, turns out to be particularly appropriate in response surface design, and allows to estimate a second order (quadratic) model for the response variable without needing of investigating the whole space of the input quantities. To this aim, only a limited number of experiments is needed and, once executed them, linear regression techniques are applied to identify the model. As it can be expected, the complexity of the model/design changes based according to number of considered input quantities; nevertheless, the sampling scheme of the input quantities space remain the same and, for the sake of the clarity, it is shown in Fig. 3.15 with reference to an example involving two independent variables. From an operating point of view, CCD can be considered as the union of three distinct sets of experimental runs:

- a set of center points (indicated by $\star$ markers in Fig. 3.15) replicated to preliminarily estimate the uncertainty of the experiment. The experimental runs are characterized by the same values of each input quantity; the adopted value turns out to be equal to the mean of the values assumed by the same quantity in the other experimental runs.

- A set of axial points (indicated by $\bullet$ markers in Fig. 3.15) capable of emulating a one-factor-at-time analysis, i.e. the quantities values are the same of the center points but for one of them, which assumes either the maximum or minimum value of the variation range.

- A set of values characterizing a typical factorial design (indicated by $\blacksquare$ markers in Fig. 3.15) where each quantity is investigated on a two levels range.

For the sake of simplicity, the values of the input quantities are usually codified in arbitrary unit; as an example, for two-parameters analysis, the coded

Table 3.7: Example CCD experiments design for 2 parameters, X_1 and X_2; α stands for coded value $\sqrt{2}$. Latin numbers identify the specific run; runs from 9^{th} to 16^{th} are carried out with the same values of input quantities.

Par.	I	II	III	IV	V	VI	VII	VIII	IX-XVI
X_1	-1	-1	1	1	$-\alpha$	α	0	0	0
X_2	-1	1	-1	1	0	0	$-\alpha$	α	0

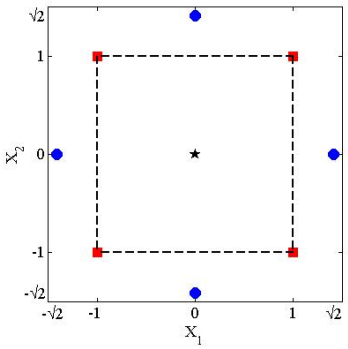

Figure 3.15: Traditional representation of values of two parameters CCD.

values are $\left[-\sqrt{2}, -1, 0, 1, \sqrt{2}\right]$. Straightforward relationships allow to determine the corresponding actual test values. The CCD experimental runs can be represented as a matrix (e.g.Table 3.7) whose columns set the values of each quantity in the corresponding experiment; the obtained results, in terms of estimated or measured performance factor, are collected and adopted to estimate the surface model.

In particular, according to the CCD theory, the surface model can be expressed as:

$$Y = b_0 + b_1 \cdot X_1 + b_2 \cdot X_2 + b_3 \cdot X_1^2 + b_4 \cdot X_2^2 + b_5 \cdot X_1 \cdot X_2 \qquad (3.4)$$

The coefficients b_i can, finally, be determined through traditional least square approaches applied to the equations system associated with the CCD experimental plan. If required, sensitivity values can easily be calculated from the coefficient b_i through the model derivative with respect to the quantity of interest.

3.5 Numerical Results

According to what stated above, a multidimensional input space involving the five considered parameters has been investigated, i.e. number of masks rows, number of masks columns, masks rotation, masks translation and, finally, threshold level. Variation ranges have been set according to the experience and the best knowledge of typical values in actual experimental tests. As for the number of masks, the traditional CS constraints for the reliable reconstruction have been taken into account. With regard to geometrical parameters (rotation and translation of the masks matrix), the adopted parameters boundaries have been chosen in such a way to avoid trivial reconstruction degradation, thus assuring the possibility of grating a sensitivity analysis to be carried out within the considered boundaries.
According to successive experimental tests, a square hole 2x2 pixels in a 10x10 pixels background has been chosen as target image. The adopted dimension granted, in fact, a suitably low sparsity K thus allowing to satisfy CS constraint 1.20 with a reduced value of M masks. Other target images characterized by the same sparsity but several non-connected regions (as an example, 4 separated pixels) have been discarded due to the high risk of reconstruction artifacts associated with thresholding operations. Finally, larger images with much more details were not appropriate to assess the configuration of the THz imaging system, since the higher number of required masks with respect to the adopted hole could make it difficult to single out the effect of the considered uncertainty sources.
Table 3.8 reports the parameters values adopted in the CCD-based runs. A number of masks between 4 and 36 has been set. In order to detect eventual influences due to the masks movement system, the tests have been carried out for different values of vertical and horizontal movements. In particular, the number of masks vertically moved (referred as "row masks" in the following) has been set equal to 2, 3 and 4. For each row value, the number of masks horizontally moved (referred as the "column masks" in the following), has been varied from 2 to 9.
The obtained results in term of MSE and $SSIM$ are presented in Table 3.9. As it can be appreciated, MSE values slightly differ from each another, thus highlighting a reduced sensitivity and inadequacy to act as proper performance factor in the assessment of CS-based THz Imaging system. On the contrary, $SSIM$ results varied within a wide range, thus allowing to define clearly the experimental configurations characterized by a suitable reconstruction of the target image.

Table 3.8: Actual values of parameters adopted for numerical tests.

Par.	$-\alpha$	-1	0	1	α
Rotation $[^\circ]$	0	0.5	1	0.5	2
Translation $[mm]$	0	0.25	0.5	0.75	1
Rows	2	3	4	5	6
Columns	2	4	6	8	10
Threshold $[\%]$	50	60	70	80	90

A more clear comparison can be carried out if a graphical representation of the multidimensional surface provided by the CCD is taken into account. Due to the multidimensional nature of the adopted approach, 3-dimensional volumetric plots are presented by setting the values of two input parameters; the value of the performance factors is associated with different colors, and the corresponding legend is given in each figure. As an example, in Fig. 3.16 the evolution of the $SSIM$ versus threshold level and number of masks rows and columns is shown; rotation and translation are set equal respectively to 0.5° and 1 mm. The $SSIM$ values are shown by means of orthogonal slice planes through the volumetric data; in particular, a defined, yellow, region of input space can be detected, capable of assuring suitable results in terms of reconstruction accuracy, in fact along all the 4^{th} row the $SSIM$ value arrives to value of $0.6-0.8$, showing also in this case a not suitable influence of the thresholding process.

According to the traditional CS theory, the higher the number of adopted masks, the better the resulting image reconstruction. Unfortunately, due to the misalignment conditions, the optimal number of masks depends also from the specific combinations of row and columns. For the sake of the clarity, Fig. 3.17 shows the evolution of the estimated $SSIM$ surface versus the number of rows and columns of the considered masks matrix, with the value of threshold level set equal to 50 %, 70 % and 90 %. To better compare the surfaces, figures have been represented with the same scale and color map. The absolute $SSIM$ maximum is achieved by means of 16 masks, arranged in 4 rows and 4 columns. A similar number of masks, 16, obtained through 2 rows and 8 columns results, instead, in a hard degradation of the reconstructed image, as shown in Fig. 3.18 with reference to a threshold value equal to 70%.

With regard to the threshold level, Fig. 3.16 suggested that the performance factor $SSIM$ slightly improve with its value.

Table 3.9: Results of MSE and $SSIM$ obtained in CCD-based tests.

Run	Rot.	Trans.	Rows	Col.	Thr.	$SSIM$	MSE
1	-1	-1	-1	-1	1	0.2530	0.04
2	-1	-1	-1	1	-1	0.5329	0.02
3	-1	-1	1	-1	-1	0.5306	0.03
4	-1	-1	1	1	1	0.1948	0.03
5	-1	1	-1	-1	-1	0.2530	0.04
6	-1	1	-1	1	1	0.1948	0.03
7	-1	1	1	-1	1	0.2424	0.05
8	-1	1	1	1	-1	0.2424	0.05
9	1	-1	-1	-1	-1	-0.0269	0.06
10	1	-1	-1	1	1	-0.0068	0.05
11	1	-1	1	-1	1	-0.0269	0.06
12	1	-1	1	1	-1	0.1661	0.07
13	1	1	-1	-1	1	-0.0068	0.05
14	1	1	-1	1	-1	-0.0068	0.05
15	1	1	1	-1	-1	-0.0457	0.07
16	1	1	1	1	1	-0.0269	0.06
17	-2	0	0	0	0	0.5329	0.02
18	2	0	0	0	0	-0.0068	0.05
19	0	-2	0	0	0	0.2424	0.05
20	0	2	0	0	0	-0.0269	0.06
21	0	0	-2	0	0	-0.0269	0.06
22	0	0	2	0	0	-0.0269	0.06
23	0	0	0	-2	0	-0.0662	0.18
24	0	0	0	2	0	0.2061	0.06
25	0	0	0	0	-2	0.2061	0.06
26	0	0	0	0	2	-0.0269	0.06

To better appreciate the superior sensitivity of the $SSIM$, in Fig. 3.19 the evolution of MSE versus the number masks rows and columns is shown in the same conditions of rotation and translation as in Fig. 3.17. Similarly to $SSIM$, also for MSE an optimal region for suitable image reconstruction, characterized by the lowest performance factor values, can be determined. Unfortunately, the MSE ranged within the interval from 0.04 up to 0.09 thus highlighting the limited sensitivity of the performance factor. This way, MSE,

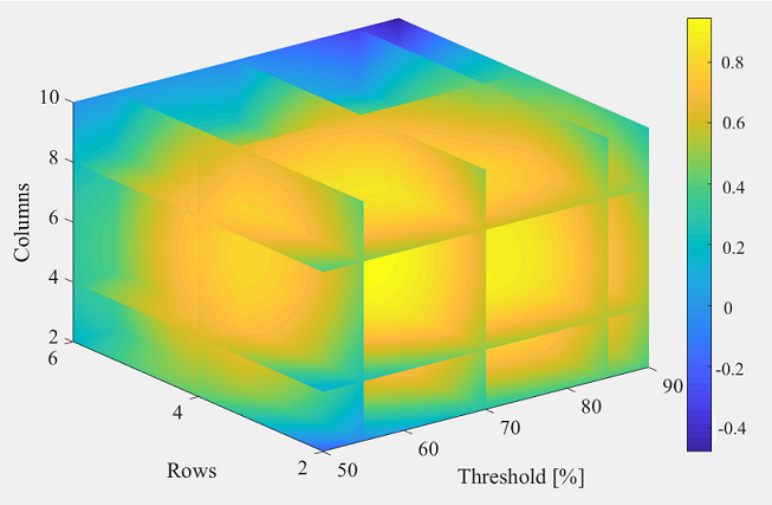

Figure 3.16: Evolution of $SSIM$ index versus threshold, row masks, and column masks.

as well as the method based on pixel difference measurement, turned out to be unfeasible as performance factor for quality analysis in THz-based Imaging systems and they are sometimes only a started point to estimate the quality of an image. This is mainly due to the adopted approach of pixel-to-pixel difference that is not capable of taking account possible target modifications such as translation or deformation.

To assess the influence of the misalignment between masks and target on the performance factor $SSIM$, further analysis have been carried out by considering its evolution versus rotation, translation and threshold level once set the number of masks rows and columns at the optimal values achieved in the previous step. To this aim, masks translation and rotation values varying within the intervals from 0 and 1 mm and from 0° to 2° has been investigated, while the number of masks was equal to 16 in a configuration of 4 rows and 4 columns. Fig. 3.20 shows the corresponding estimated values of $SSIM$, while some results in the presence of a threshold level equal to 90 % are presented in Fig. 3.21, where the evolution of the estimated $SSIM$ surface is plotted versus the masks translation and rotation. As it can be appreciated, the translation is not capable of significantly affecting the value of the performance factors, while the rotation hardly reduces the similarity between the reconstructed and target image, thus decreasing the $SSIM$, so only very small values of the rotation

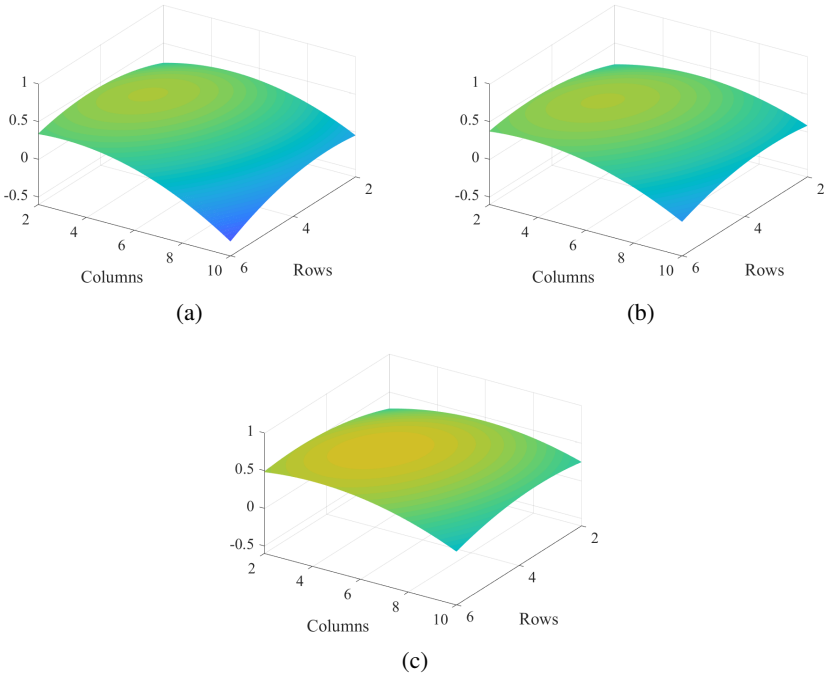

Figure 3.17: Evolution of $SSIM$ index versus column masks and row masks for different values of threshold a) 50% b) 70% c) 90%.

factor are acceptable to assure significant index and, consequently, accurate reconstructions.

Finally, in the Fig. 3.20 the numerical tests have also shown the effect of thresholding process, in which it does not improve the $SSIM$ index values, in fact until the threshold values are little, (i.e 50 %-65 %) the $SSIM$ has values tending to acceptable values represented by the yellow color of the legend, while for high threshold values there is not an improvement of the index value but a wrong reconstruction of the image is obtained.

3.6 Experimental Tests

Experimental tests have been realized to justify numerical results, in particular THz system, considered for analysis, has been described in section 3.1, the set of M random masks has been described carefully in section 2.3, while to assure a suitable control on the uncertainty sources and with no loss of

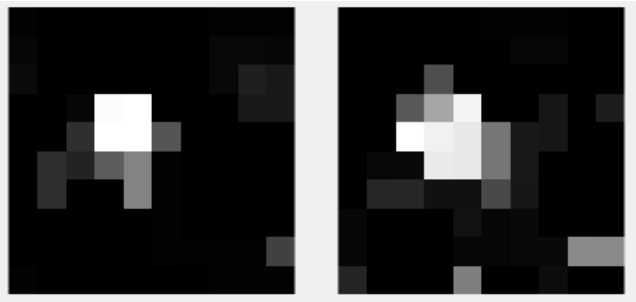

Figure 3.18: Reconstructed images obtained with 16 masks; on the left by adopting 4 row masks and 4 column masks, on the right by adopting 2 row masks and 8 column masks.

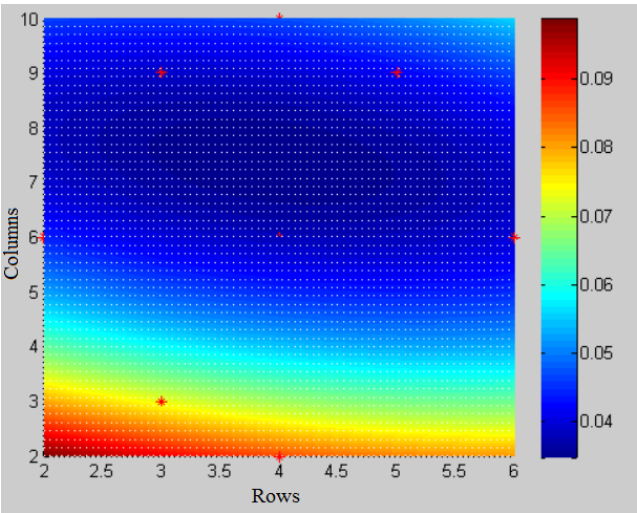

Figure 3.19: Evolution of MSE index versus row masks and column masks.

significance, the sample under test (i.e. the target) for the experimental characterization has been obtained by creating a square hole, whose size is 2x2 mm^2, in a sheet of cardboard covered by metallic scotch tape whose dimensions were equal to 10x10 mm^2.

Some figures about experimental results are presented, in particular the value assumed by the indexes $SSIM$ and MSE versus the number of masks,

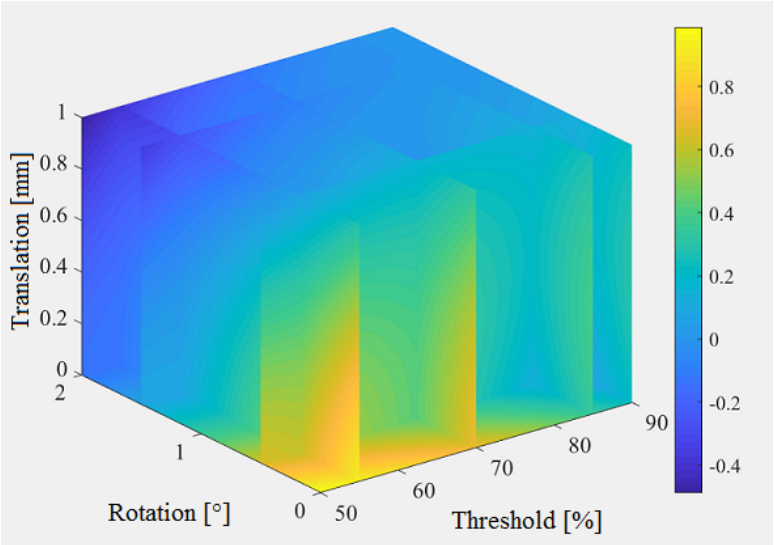

Figure 3.20: Evolution of $SSIM$ index versus threshold value, mask's rotation, and mask's translation

in all the described conditions. In each graph, the number of column masks is reported on x axis, whereas on y axis the value of the quality index is shown. The three curves are referred to the three values of row masks.
It has to be noted that the best value of MSE is 0, because it means that the reconstructed image and the reference one are perfectly equal, and for SSIM index the best value is 1, which states the perfect similarity between the reconstructed and the reference images.
In Fig. 3.22a the evolution of MSE and $SSIM$ is shown, when the image has been processes with a 90 % threshold.
The MSE reaches values lower than 0.1 when a number of mask equal or greater than 8 is adopted. In fact, 2x4, 3x3 and 4x2 masks assures a notable concurrence with the reference image. According to the MSE evolution, if a greater number of masks is chosen, the error between the reconstructed and reference images remain almost constant. A large number of masks, then, makes the capture time much longer, but does not provide a better reliability of the reconstruction.
As regards the $SSIM$ index, it reaches its maximum value of 0.53 with 4x5 masks. It is worth noting that, the increase of the number of masks and so

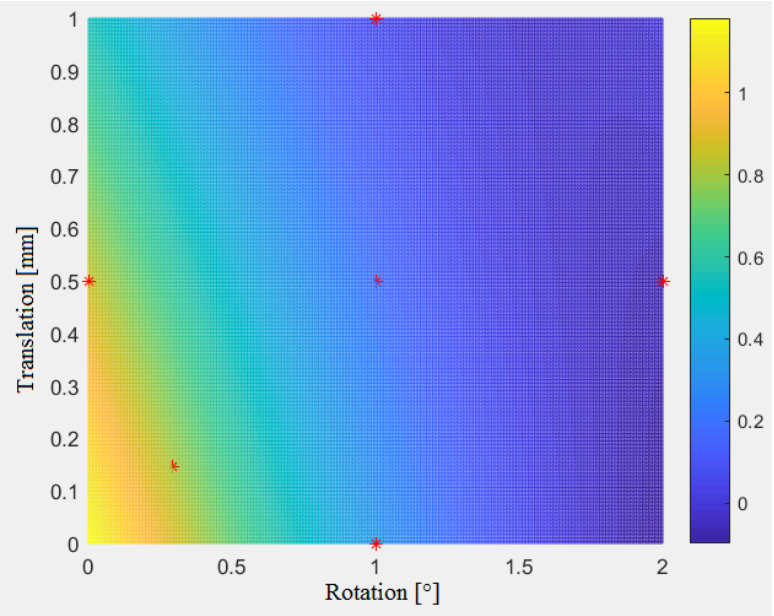

Figure 3.21: Evolution of $SSIM$ index versus masks's rotation and masks's traslation with 16 masks considered.

of measurements causes the deterioration of $SSIM$ index. This behavior is due to an alignment error of the masks, because of two effects: (i) the sheet containing the 100 masks is not perfectly align with the THz beam; (ii) the stepper motors move the sheet of a quantity, which does not exactly match the distance between the center of the masks. In both cases, when the measurements performed with different masks are processed through the CS algorithm, a reconstruction error is observed. This error is strictly dependent on the number of masks involved, thus the quality of reconstruction can get worse if the number of masks increase. Moreover, since not all uniform distribution binary matrix can be used as measurement matrix for CS-based imaging purposes [80],[81], further tests has been conducted by rotating the masks matrix by 90, 180 and 270 degrees in order to avoid confounding possible artifacts due to the unsuitability of some adopted random masks. If this was case, the harmful effects associated with unsuitable masks should be first evidenced with respect to the results presented in Fig. 3.22. Nevertheless, no significant differences have been encountered, thus assuring the main role of the mask misalignment

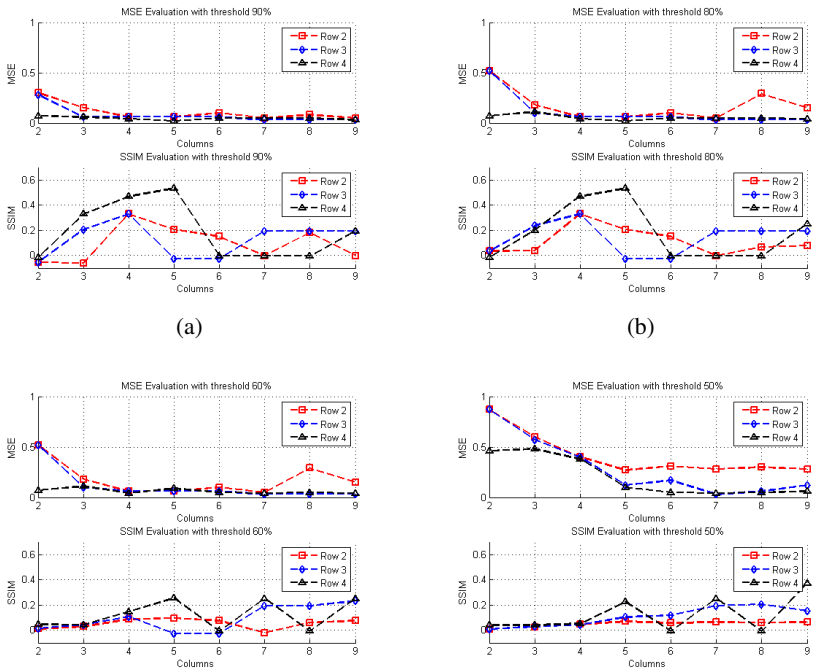

(a) (b)

(c) (d)

Figure 3.22: Evolution of MSE and $SSIM$ versus the number of column masks, with threshold equal to 90 % (a), 80 % (b), 60 % (c), and 50 % (d), respectively.

on the optimal number and arrangement of the masks and, consequently, the reconstruction quality.
A similar situation can be appreciated in Fig. 3.22b, where the threshold has been set to 80 %. Acceptable values of MSE index can be obtained just with 4 column masks. When 8 column masks are used, especially with only 2 row masks, also the MSE index exhibits a detriment due to the alignment error previously discussed. In this tests, in fact, the threshold has been lowered and, therefore, a larger number of grey pixels due to the alignment error are forced to 1.
The $SSIM$ index, similarly to the previous graph, increase with the number of column masks, reaches its maximum value in correspondence of 20 masks and it deteriorates if a large number of column masks is adopted.
Reducing the threshold value, from 60 % to 50 %, as Fig. 3.22c and Fig. 3.22d shown, a deterioration of both indexes is appreciated. This effect is related to an increasing number of pixels that have a value greater than the threshold and so these aspects invalidate the reconstruction and the evaluation of the indexes.
Finally, in Fig. 3.23 an overview of the obtained results is shown in particular for a threshold equal to 90 %. The number of optimal masks is about 5 times the area of the defect expressed in pixels, in this case equal to 20 masks. It should be noted, however, that the quality of the reconstruction is not independent on the arrangement of the masks; the image obtained with 2x8 masks does not exhibit the same quality of the image obtained with 4x4 masks. In order to minimize the effect of the error of alignment, the best arrangement is the one that minimizes the stroke to be made by the stepper motor, so the arrangement of the masks has to tend towards a square.
Concerning the index to be taken into account as the reliability indicator, in tests for the detection of defects, the $SSIM$ index is strongly preferred. As an example, in Fig. 3.24 reconstructed images of a T letter achieved in different configuration of the Imaging system in terms of rotation and translation of the CS masks are shown. All the reconstructed images have been obtained considering a threshold value of 30%. In each test, the $SSIM$ of reference 2x2 mm^2 square hole has been preliminary evaluated. The reliable reconstruction of Fig. 3.24.a. has been obtained after carefully aligning the CS masks, as confirmed by $SSIM$ value as high as 0.96. Similar results are achieved if a horizontal translation of 1 mm with respect to the center of the THz beam is considered (Fig. 3.24.b). Reconstruction quality degraded when a rotation of the CS masks is added; in particular, Fig. 3.24.c, figure 3.24.d and Fig. 3.24.e correspond to couples of values of rotation and translation equal respectively

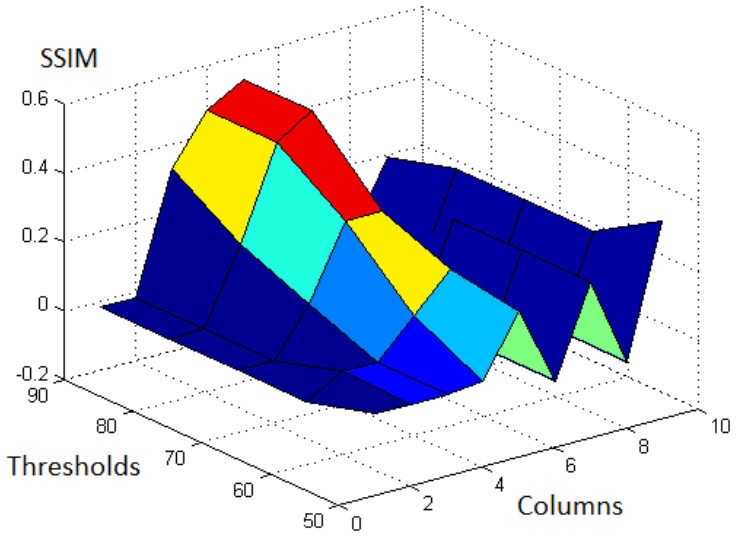

Figure 3.23: Evolution of SSIM index with a number of row masks equal to 4.

to (0.5°,0 mm),(0.5°,1 mm) and (1°,1 mm). $SSIM$ values never greater of 0.32 have been encountered in these last three cases, thus highlighting the suitability of the considered performance factor in detecting incorrect configurations of the Imaging system resulting in unreliable reconstructed images. The tests have been conducted by first setting the zero rotation condition by means of traditional gauge blocks for parallelism monitoring and adopting a suitable laser facility of the THz imaging system for the center alignment of masks and target. Successively, suitable programming of the step motors allowed to emulate the translation up to 2 mm between nominal and actual mask position, while the rotation of the masks matrix has been accurately checked and controlled through a proper goniometer stage GNL18 by Thorlabs (full scale and resolution equal respectively to $\pm 5°$ and $0.167°$).

Finally, results of a comparison between the reconstruction of a defect obtained with the simple RS technique and CS-approach are shown. In particular, the defect is represented by a square hole of $3x3mm^2$, realized on a piece of

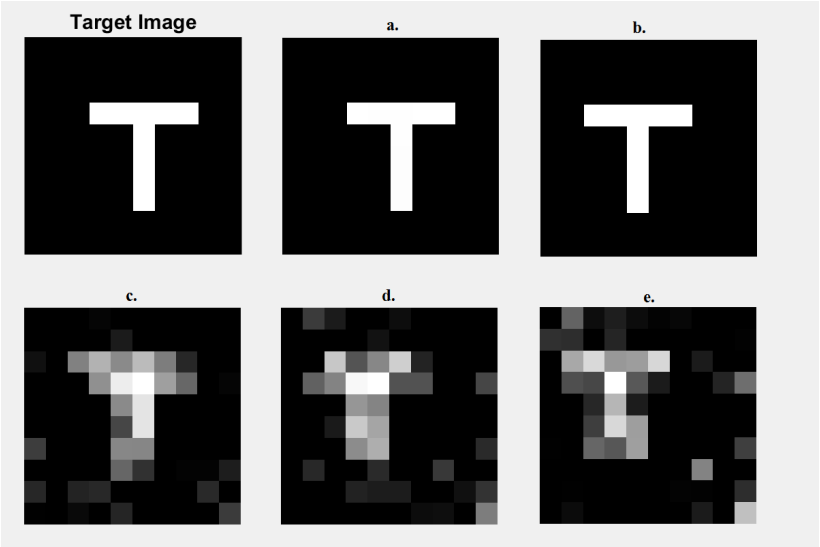

Figure 3.24: Reconstruction of T Letter with threshold value of 30%: case a.) Angle = 0° and Translation = 0 mm; case b.) Angle = 0° and Translation = 1 mm; case c.) Angle = 0.5° and Translation = 0 mm; case d.) Angle = 0.5° and Translation = 1 mm; case e.) Angle = 1° and Translation = 1 mm

Kevlar; the RS is shown in Fig. 3.25a and compared with reconstruction obtained with CS-approach considering 9x4 masks (3.25b). At the same time, the image of the same hole hidden between two layers of concrete wall (total thickness 7.45 mm) is shown in Fig. 3.25c for RS and Fig. 3.25d for CS.

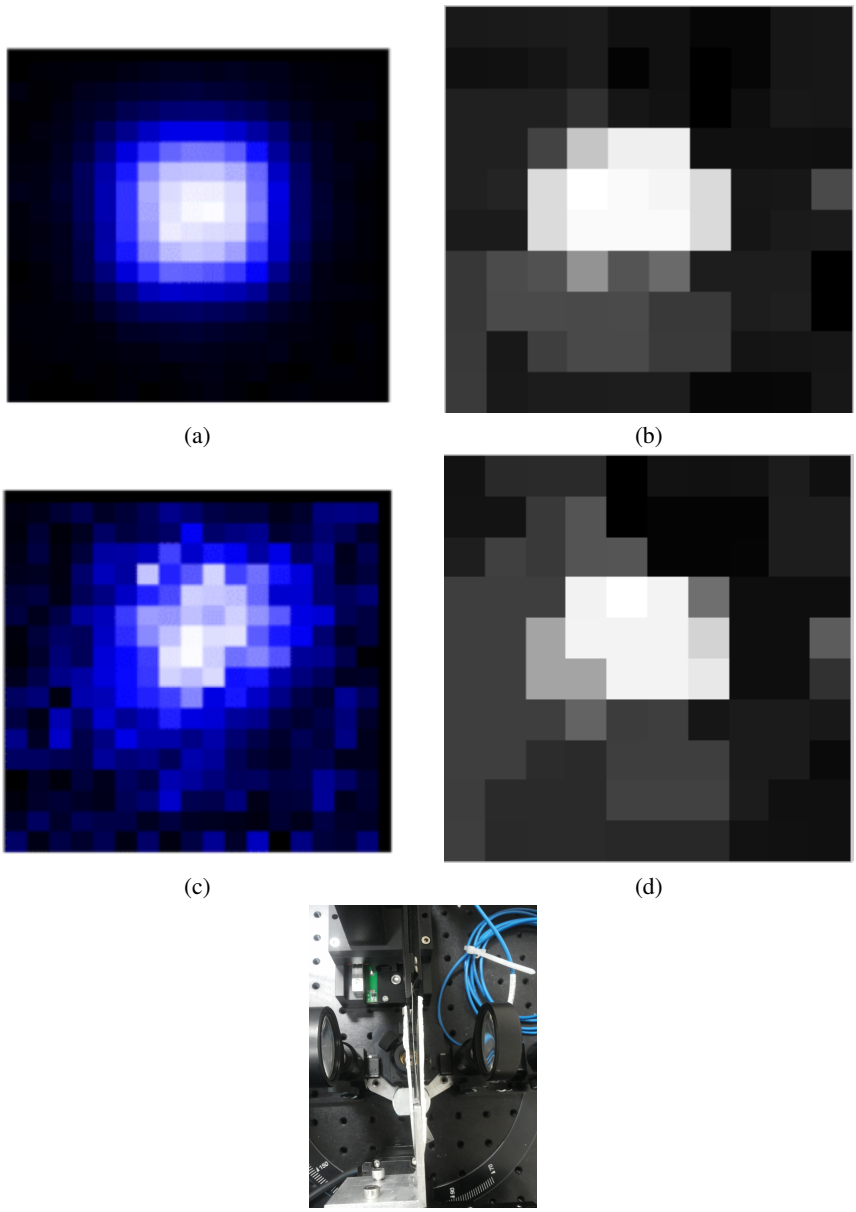

(a) (b) (c) (d) (e)

Figure 3.25: (a) Raster Scan THz imaging of a hole $3x3mm^2$;(b) CS-THz Imaging of the hole; (c) Raster Scan of the same hole hidden between two layers of concrete wall with a total thickness of 7.45 mm. In both images, spatial resolution is 0.4 mm; (d) CS-THz Imaging of the same hole hidden; (e) top view of two layers in which the hole is hidden

Chapter 4

Conclusions

This thesis work involved the treatment of non-destructive and non-invasive tests, which, in recent years, have become increasingly relevant in the different fields of research and development, and in particular in the engineering world. The importance of this argument is linked to the fact that cracking defects can affect performance in a devastating way. Very often, NTC applications are thought to have application for detecting and localizing defects, in the truth they cover much wider aspects such as the morphological and structural study of the component under investigation, or the physico-chemical properties analysis, preparation methods and others. A lot are the NDT techniques that could be consider as X-rays, ultrasonics, penetration with penetrating liquids, thermography and others. To these traditional techniques, two alternative methods have been introduced and presented THz technology, with a particular attention to THz Spectroscopy and Imaging, taking into account the good properties of T-waves, and Eddy Current Testing (ECT). Both methods have benefited from their application of a new sampling approach, which goes under name of compressed sampling (CS) and which is designed to go beyond the boundaries imposed by the Nyquist-Shannon theorem. In particular, an experimental investigation about the effects of configuration parameters in CS-based THz imaging systems has been presented, focusing attention on the influence that quantities associated with the application of the compressive sampling have on the final quality of reconstructed images in THz systems. Stemming from a deep analysis of the measurement process associated with the operating steps of the CS-based THz imaging, the main uncertainty sources (except those associated with THz beam generation and acquisition) have been singled out and their effect estimated thanks to a

suitable design of experiments approach. In particular, the first considered source has been the misalignment of the matrix of masks usually adopted in CS-based THz imaging applications with respect with its ideal configuration; to this aim angular rotation and linear translation of the matrix have been taken into account. Moreover, number of different masks adopted to arrange the so-called sensing matrix has been considered. Finally, the effect of threshold level for image enhancement have been investigated.

A number of tests conducted both in numerical and actual experiments have been carried out to assess the uncertainty sources effects. As regards the numerical tests, two performance factors, referred to as $SSIM$ and MSE, have been considered in order to quantify the quality of reconstructed images. Both factors have been calculated with reference to a common target image consisting of a square hole; MSE is based on pixels difference measurements, while $SSIM$ exploited a human visual approach to estimate quality measurements. Central composite design has been adopted in order to efficiently estimate the evolution response surface of two performance factors versus the considered uncertainty sources.

Obtained results have highlighted that (*i*) $SSIM$ provides better performance due to sensitivity values higher than those granted by MSE, (*ii*) angular rotation of the masks matrix has been identified as the most influencing source, (*iii*) moderated value of horizontal or vertical translation only resulted in translation of the reconstructed images with respect to the ideal center, (*iv*) an optimal number of masks could be determined for target reconstruction and (*v*) also the position of the masks within the matrix has been assessed as uncertainty sources. With specific regard to the last two items, differently from the ideal application of the CS approach, increasing number of masks adopted for images reconstruction did not correspond to continuous improvement of their quality. Moreover, given the optimal number of masks, the best configuration is given by a "square" of masks in the matrix; this configuration, in fact, minimize the effect of the misalignment uncertainty sources.

Numerical results have been confirmed by the tests conducted by means of an actual CS-based THz imaging system. In particular, $SSIM$ values obtained with the reference square-hole target have been adopted as road-map to correctly align the masks matrix. Some results shown in the paper about the reconstruction of T-shaped hole clearly highlighted the efficacy of the proposed approach. At the same time, CS approach has been applied in Eddy Current Testing in order to overcome the drawbacks introduced by this technique, as the requirement of large amounts of memory to store and save the acquired

data and long time intervals for acquisition and reconstruction signal. These limits born because it is common to divide the various testing areas into micro structures, each of which is in turn considered to be a sub-pixel structure. For each pixel, according to the theory of ECT, it is necessary to acquire two signals that the probes can detect, i.e voltage and current, necessary to extract the information necessary to confirm the presence or not of the defect inside the structure. The electrical signals are captured with a very large number of samples, about 100,000 samples per pixel, taking into account the time needed to capture all these samples. In this thesis it has been shown that CS approach permits to reduce the amount of data to be captured and stored in the memory slots, and at the same time reduce the acquisition and subsequent reconstruction of the signal. The analysis has been conducted taking into account two particular CS-Solver, that have permitted to obtained very little time interval for reconstructed signal, about 1 s for MP-solver and 0.5 s for CoSaMP-solver, values obtained also considering particular graphics solutions as *CUDA-GPU*. About value of samples for reconstruction process is possible to consider as best value about 300-350 samples.

Bibliography

[1] Giovanni Betta, Luigi Ferrigno, and Marco Laracca. Gmr-based ect instrument for detection and characterization of crack on a planar specimen: A hand-held solution. *IEEE transactions on instrumentation and measurement*, 61(2):505–512, 2012.

[2] Andrea Bernieri, Giovanni Betta, Luigi Ferrigno, and Marco Laracca. Crack depth estimation by using a multi-frequency ect method. *IEEE Transactions on Instrumentation and Measurement*, 62(3):544–552, 2013.

[3] Peter H Siegel. Thz technology: An overview. *International Journal of High Speed Electronics and Systems*, 13(02):351–394, 2003.

[4] YC Shen, a T Lo, PF Taday, BE Cole, WR Tribe, and MC Kemp. Detection and identification of explosives using terahertz pulsed spectroscopic imaging. *Applied Physics Letters*, 86(24):241116, 2005.

[5] Philip F Taday. Applications of terahertz spectroscopy to pharmaceutical sciences. *Philosophical Transactions of the Royal Society of London A: Mathematical, Physical and Engineering Sciences*, 362(1815):351–364, 2004.

[6] Lindsay Owens, Douglas T Petkie, and Jason A Deibel. Non-destructive evaluation of aerospace materials using terahertz time-domain imaging. In *Optical Sensors*, pages SW4C–4. Optical Society of America, 2012.

[7] GJ Wilmink and JE Grundt. Terahertz radiation: Sources, applications, and biological effects. *Electromagnetic Fields in Biological Systems*, pages 369–423, 2012.

[8] Aurele Joseph Louis Adam. Review of near-field terahertz measurement methods and their applications. *Journal of Infrared, Millimeter, and Terahertz Waves*, 32(8-9):976, 2011.

[9] Albert Redo-Sanchez, Norman Laman, Brian Schulkin, and Thomas Tongue. Review of terahertz technology readiness assessment and applications. *Journal of Infrared, Millimeter, and Terahertz Waves*, 34(9):500–518, 2013.

[10] RM Woodward, VP Wallace, DD Arnone, EH Linfield, and M Pepper. Terahertz pulsed imaging of skin cancer in the time and frequency domain. *Journal of Biological Physics*, 29(2-3):257–259, 2003.

[11] Leopoldo Angrisani, Giovanni Cavallo, Annalisa Liccardo, Gian Paolo Papari, and Antonello Andreone. Thz measurement systems. In *New Trends and Developments in Metrology*. InTech, 2016.

[12] Zoya Popovic and Erich N Grossman. Thz metrology and instrumentation. *IEEE Transactions on Terahertz Science and Technology*, 1(1):133–144, 2011.

[13] Masanori Hangyo. Development and future prospects of terahertz technologythis is a translated version of the original paper which appeared in oyo buturi 81, 271 (2012)[in japanese]. *Japanese Journal of Applied Physics*, 54(12):120101, 2015.

[14] Lionel Duvillaret, Frédéric Garet, and J-L Coutaz. A reliable method for extraction of material parameters in terahertz time-domain spectroscopy. *IEEE Journal of selected topics in quantum electronics*, 2(3):739–746, 1996.

[15] Hiroaki Yasuda and Iwao Hosako. Measurement of terahertz refractive index of metal with terahertz time-domain spectroscopy. *Japanese Journal of Applied Physics*, 47(3R):1632, 2008.

[16] Da-xiang Zhou, Edward PJ Parrott, Douglas J Paul, and J Axel Zeitler. Determination of complex refractive index of thin metal films from terahertz time-domain spectroscopy. *Journal of Applied Physics*, 104(5):053110, 2008.

[17] Timothy D Dorney, Richard G Baraniuk, and Daniel M Mittleman. Material parameter estimation with terahertz time-domain spectroscopy. *JOSA A*, 18(7):1562–1571, 2001.

[18] Ioachim Pupeza, Rafal Wilk, and Martin Koch. Highly accurate optical material parameter determination with thz time-domain spectroscopy. *Optics express*, 15(7):4335–4350, 2007.

[19] Maik Scheller, Christian Jansen, and Martin Koch. Analyzing sub-100-μm samples with transmission terahertz time domain spectroscopy. *Optics Communications*, 282(7):1304–1306, 2009.

[20] Withawat Withayachumnankul, Bernd M Fischer, and Derek Abbott. Material thickness optimization for transmission-mode terahertz time-domain spectroscopy. *Optics express*, 16(10):7382–7396, 2008.

[21] P Kužel and H Němec. Terahertz conductivity in nanoscaled systems: effective medium theory aspects. *Journal of Physics D: Applied Physics*, 47(37):374005, 2014.

[22] Ivan Ivanov, Mischa Bonn, Zoltán Mics, and Dmitry Turchinovich. Perspective on terahertz spectroscopy of graphene. *EPL (Europhysics Letters)*, 111(6):67001, 2015.

[23] AK Denisultanov, SE Azbite, NS Balbekin, SI Gusev, and MK Khodzitsky. Optical properties of graphene on quartz and polyethylene substrates in terahertz frequency range. *PIERS Proc*, pages 2022–2025, 2014.

[24] JB Jackson, M Mourou, JF Whitaker, I NIII Duling, SL Williamson, M Menu, and GA Mourou. Terahertz imaging for non-destructive evaluation of mural paintings. *Optics communications*, 281(4):527–532, 2008.

[25] Jason Bassi, Mira Naftaly, Bob Miles, and Yang Zhang. The investigation of sooty flames using terahertz waves. *Flow measurement and instrumentation*, 16(5):341–345, 2005.

[26] A. Bernieri, G. Betta, and L. Ferrigno. Characterization of an eddy-current-based system for nondestructive testing. *IEEE Transactions on Instrumentation and Measurement*, 51(2):241–245, 2002.

[27] Andrea Taschin, Paolo Bartolini, Jordanka Tasseva, and Renato Torre. {THz} time-domain spectroscopic investigations of thin films. *Measurement*, pages –, 2017.

[28] BB Hu and MC Nuss. Imaging with terahertz waves. *Optics letters*, 20(16):1716–1718, 1995.

[29] Nicholas Karpowicz, Hua Zhong, Jingzhou Xu, Kuang-I Lin, Jenn-Shyong Hwang, and XC Zhang. Comparison between pulsed terahertz time-domain imaging and continuous wave terahertz imaging. *Semiconductor Science and Technology*, 20(7):S293, 2005.

[30] Torsten Löffler, Thilo May, Christian am Weg, Ali Alcin, Bernd Hils, and Hartmut G Roskos. Continuous-wave terahertz imaging with a hybrid system. *Applied Physics Letters*, 90(9):091111, 2007.

[31] L Angrisani, F Bonavolontà, R Schiano Lo Moriello, A Andreone, R Casini, G Papari, and D Accardo. First steps towards an innovative compressive sampling based-thz imaging system for early crack detection on aereospace plates. In *Metrology for Aerospace (MetroAeroSpace), 2014 IEEE*, pages 488–493. IEEE, 2014.

[32] DC Jiles. Review of magnetic methods for nondestructive evaluation (part 2). *NDT international*, 23(2):83–92, 1990.

[33] Giovanni Betta, Pietro Burrascano, Luigi Ferrigno, Marco Laracca, Marco Ricci, and Giuseppe Silipigni. An experimental comparison of complex excitation sequences for eddy current testing. *ACTA IMEKO*, 4(1):128–134, 2015.

[34] Giovanni Betta, Pietro Burrascano, Luigi Ferrigno, Marco Laracca, Marco Ricci, and Giuseppe Silipigni. On the use of complex excitation sequences for eddy current testing. In *Proceeding of 19th IMEKO TC4 Symposium, Barcelona, Spain*, pages 410–415, 2013.

[35] Manfred Schroeder. Synthesis of low-peak-factor signals and binary sequences with low autocorrelation (corresp.). *IEEE Transactions on Information Theory*, 16(1):85–89, 1970.

[36] Harry Nyquist. Certain topics in telegraph transmission theory. *Transactions of the American Institute of Electrical Engineers*, 47(2):617–644, 1928.

[37] Emmanuel J Candès and Michael B Wakin. An introduction to compressive sampling. *IEEE signal processing magazine*, 25(2):21–30, 2008.

[38] Emmanuel J Candès et al. Compressive sampling. In *Proceedings of the international congress of mathematicians*, volume 3, pages 1433–1452. Madrid, Spain, 2006.

[39] Emmanuel J Candès, Justin Romberg, and Terence Tao. Robust uncertainty principles: Exact signal reconstruction from highly incomplete frequency information. *IEEE Transactions on information theory*, 52(2):489–509, 2006.

[40] Emmanuel J Candes and Terence Tao. Near-optimal signal recovery from random projections: Universal encoding strategies? *IEEE transactions on information theory*, 52(12):5406–5425, 2006.

[41] Emmanuel Candes and Justin Romberg. Sparsity and incoherence in compressive sampling. *Inverse problems*, 23(3):969, 2007.

[42] Dave Mesecher, Larry Carin, Ivan Kadar, and Ron Pirich. Exploiting signal sparseness for reduced-rate sampling. In *Systems, Applications and Technology Conference, 2009. LISAT'09. IEEE Long Island*, pages 1–6. IEEE, 2009.

[43] David L Donoho. Compressed sensing. *IEEE Transactions on information theory*, 52(4):1289–1306, 2006.

[44] Wotao Yin, Stanley Osher, Donald Goldfarb, and Jerome Darbon. Bregman iterative algorithms for \ell_1-minimization with applications to compressed sensing. *SIAM Journal on Imaging sciences*, 1(1):143–168, 2008.

[45] Mohammed M Abo-Zahhad, Aziza I Hussein, and Abdelfatah M Mohamed. Compressive sensing algorithms for signal processing applications: A survey. *International Journal of Communications, Network and System Sciences*, 8(06):197, 2015.

[46] Antonin Chambolle, Vicent Caselles, Daniel Cremers, Matteo Novaga, and Thomas Pock. An introduction to total variation for image analysis. *Theoretical foundations and numerical methods for sparse recovery*, 9(263-340):227, 2010.

[47] Antonin Chambolle. An algorithm for total variation minimization and applications. *Journal of Mathematical imaging and vision*, 20(1):89–97, 2004.

[48] Chengbo Li. *An efficient algorithm for total variation regularization with applications to the single pixel camera and compressive sensing*. PhD thesis, Rice University, 2010.

[49] Shuying Yang, Karen Lozano, Azalia Lomeli, Heinrich D Foltz, and Robert Jones. Electromagnetic interference shielding effectiveness of carbon nanofiber/lcp composites. *Composites Part A: applied science and manufacturing*, 36(5):691–697, 2005.

[50] Mohammed H Al-Saleh and Uttandaraman Sundararaj. Electromagnetic interference shielding mechanisms of cnt/polymer composites. *Carbon*, 47(7):1738–1746, 2009.

[51] Simon Rea, David Linton, Eddie Orr, and Jonathan McConnell. Electromagnetic shielding properties of carbon fibre composites in avionic systems. *Mikrotalasna revija*, 11(1):29–32, 2005.

[52] J Macutkevic, D Seliuta, G Valusis, R Adomavicius, P Kuzhir, A Paddubskaya, M Shuba, S Maksimenko, L Coderoni, F Micciulla, et al. Terahertz time domain spectroscopy of epoxy resin composite with various carbon inclusions. *Chemical Physics*, 404:129–135, 2012.

[53] MA Seo, JH Yim, YH Ahn, F Rotermund, DS Kim, S Lee, and H Lim. Terahertz electromagnetic interference shielding using single-walled carbon nanotube flexible films. *Applied Physics Letters*, 93(23):231905, 2008.

[54] Michael FL De Volder, Sameh H Tawfick, Ray H Baughman, and A John Hart. Carbon nanotubes: present and future commercial applications. *science*, 339(6119):535–539, 2013.

[55] Lei Ren, Cary L Pint, Layla G Booshehri, William D Rice, Xiangfeng Wang, David J Hilton, Kei Takeya, Iwao Kawayama, Masayoshi Tonouchi, Robert H Hauge, et al. Carbon nanotube terahertz polarizer. *Nano letters*, 9(7):2610–2613, 2009.

[56] Jay A Berres and George W Hanson. Multiwall carbon nanotubes at rf-thz frequencies: scattering, shielding, effective conductivity, and power dissipation. *IEEE Transactions on Antennas and Propagation*, 59(8):3098–3103, 2011.

[57] Ronald Ulbricht, Euan Hendry, Jie Shan, Tony F Heinz, and Mischa Bonn. Carrier dynamics in semiconductors studied with time-resolved terahertz spectroscopy. *Reviews of Modern Physics*, 83(2):543, 2011.

[58] P Uhd Jepsen, David G Cooke, and Martin Koch. Terahertz spectroscopy and imaging–modern techniques and applications. *Laser & Photonics Reviews*, 5(1):124–166, 2011.

[59] D Grischkowsky, Søren Keiding, Martin Van Exter, and Ch Fattinger. Far-infrared time-domain spectroscopy with terahertz beams of dielectrics and semiconductors. *JOSA B*, 7(10):2006–2015, 1990.

[60] Francesco D'Angelo, Zoltán Mics, Mischa Bonn, and Dmitry Turchinovich. Ultra-broadband thz time-domain spectroscopy of common polymers using thz air photonics. *Optics express*, 22(10):12475–12485, 2014.

[61] S Wietzke, C Jansen, M Reuter, T Jung, D Kraft, S Chatterjee, BM Fischer, and M Koch. Terahertz spectroscopy on polymers: A review of morphological studies. *Journal of Molecular Structure*, 1006(1):41–51, 2011.

[62] Lionel Duvillaret, Frederic Garet, and Jean-Louis Coutaz. Highly precise determination of optical constants and sample thickness in terahertz time-domain spectroscopy. *Applied optics*, 38(2):409–415, 1999.

[63] Stéphane G Mallat and Zhifeng Zhang. Matching pursuits with time-frequency dictionaries. *IEEE Transactions on signal processing*, 41(12):3397–3415, 1993.

[64] Deanna Needell and Joel A Tropp. Cosamp: Iterative signal recovery from incomplete and inaccurate samples. *Applied and Computational Harmonic Analysis*, 26(3):301–321, 2009.

[65] Deanna Needell, Joel Tropp, and Roman Vershynin. Greedy signal recovery review. In *Signals, Systems and Computers, 2008 42nd Asilomar Conference on*, pages 1048–1050. IEEE, 2008.

[66] Deanna Needell and Roman Vershynin. Signal recovery from incomplete and inaccurate measurements via regularized orthogonal matching pursuit. *IEEE Journal of selected topics in signal processing*, 4(2):310–316, 2010.

[67] F Bonavolontà, M D'Arco, G Ianniello, A Liccardo, R Schiano Lo Moriello, L Ferrigno, M Laracca, and G Miele. On the suitability of compressive sampling for the measurement of electrical power quality. In *Instrumentation and Measurement Technology Conference (I2MTC), 2013 IEEE International*, pages 126–131. IEEE, 2013.

[68] Justin Romberg. Imaging via compressive sampling. *IEEE Signal Processing Magazine*, 25(2):14–20, 2008.

[69] Mira Naftaly. Metrology issues and solutions in thz time-domain spectroscopy: Noise, errors, calibration. *IEEE Sensors Journal*, 13(1):8–17, 2013.

[70] Withawat Withayachumnankul and Mira Naftaly. Fundamentals of measurement in terahertz time-domain spectroscopy. *Journal of Infrared, Millimeter, and Terahertz Waves*, 35(8):610–637, 2014.

[71] Yasuzi Suzaki and Atsushi Tachibana. Measurement of the μm sized radius of gaussian laser beam using the scanning knife-edge. *Applied Optics*, 14(12):2809–2810, 1975.

[72] John M Khosrofian and Bruce A Garetz. Measurement of a gaussian laser beam diameter through the direct inversion of knife-edge data. *Applied Optics*, 22(21):3406–3410, 1983.

[73] Pellegrino Musto, Pietro Russo, Francesca Cimino, Domenico Acierno, Giovanni Lupò, and Carlo Petrarca. Dielectric behavior of biopolymer based composites containing multi wall carbon nanotubes: Effect of filler content and aspect ratio. *European Polymer Journal*, 64:170–178, 2015.

[74] Debanjan Polley, Anjan Barman, and Rajib Kumar Mitra. Controllable terahertz conductivity in single walled carbon nanotube/polymer composites. *Journal of Applied Physics*, 117(2):023115, 2015.

[75] Debanjan Polley, Kumar Neeraj, Anjan Barman, and Rajib Kumar Mitra. Diameter-dependent shielding effectiveness and terahertz conductivity of multiwalled carbon nanotubes. *JOSA B*, 33(12):2430–2436, 2016.

[76] Qi Zhang, Erik H Hároz, Zehua Jin, Lei Ren, Xuan Wang, Rolf S Arvidson, Andreas Lüttge, and Junichiro Kono. Plasmonic nature of the terahertz conductivity peak in single-wall carbon nanotubes. *Nano letters*, 13(12):5991–5996, 2013.

[77] Yusra AY Al-Najjar and D Chen Soong. Comparison of image quality assessment: Psnr, hvs, ssim, uiqi. *International Journal of Scientific & Engineering Research*, 3(8):1, 2012.

[78] Zhou Wang, Alan C Bovik, Hamid R Sheikh, and Eero P Simoncelli. Image quality assessment: from error visibility to structural similarity. *IEEE transactions on image processing*, 13(4):600–612, 2004.

[79] Richard F Gunst. Response surface methodology: process and product optimization using designed experiments, 1996.

[80] Marco F Duarte and Yonina C Eldar. Structured compressed sensing: From theory to applications. *IEEE Transactions on Signal Processing*, 59(9):4053–4085, 2011.

[81] Arash Saber Tehrani, Alexandros G Dimakis, and Giuseppe Caire. Optimal binary measurement matrices for compressed sensing. In *Information Theory Workshop (ITW), 2013 IEEE*, pages 1–5. IEEE, 2013.